Process-based modelling of nonharmonic internal tides using adjoint, statistical, and stochastic approaches. Part II: adjoint frequency response analysis, stochastic models, and synthesis

Kenji Shimizu[1,2]

[1]Kobe University, 1-1 Rokkodai-cho, Nada-ku, Kobe, 657-8501, Japan
[2]RPS AAP Consulting Pty Ltd, 500 Hay Street, Subiaco, Western Australia, 6008, Australia

Correspondence: Kenji Shimizu (kenji.shimizu.rc@gmail.com)

Abstract. Internal tides are known to contain a substantial component that cannot be explained by (deterministic) harmonic analysis, and the remaining nonharmonic component is considered to be caused by random oceanic variability. For nonharmonic internal tides originating from distributed sources, the superposition of many waves with different degrees of randomness unfortunately makes process investigation more difficult. This paper develops a new framework for process-based modelling of nonharmonic internal tides by combining adjoint, statistical, and stochastic approaches, and uses its implementation to investigate important processes and parameters controlling nonharmonic internal-tide variance. A combination of adoint sensitivity modelling and the frequency response analysis from Fourier theory provides distributed deterministic sources of internal tides observed at a fixed location, which enables assignment of different degrees of randomness to waves from different sources. The wave phases are randomized by the statistical model from Part I, using horizontally varying phase statistics calculated by stochastic models. An example application to nonharmonic vertical-mode-one semidiurnal internal tides on the Australian North West Shelf shows that (i) phase-speed variability primarily makes internal tides nonharmonic through phase modulation, and (ii) important controlling parameters include the variance and correlation length of phase speed, as well as anisotropy of the horizontal correlation of phase modulation. The model suite also provides the map of nonharmonic internal-tide sources, which is convenient for identifying important remote sources, such as the Lombok Strait in Indonesia. The proposed modelling framework and model suite provide a new tool for process-based studies of nonharmonic internal tides from distributed sources.

Short summary

This study develops a new model suite for the random component of internal tides (internal waves at tidal frequencies). Its example application shows that important parameters for the randomization are the magnitude and correlation length of phase-speed variability, and directional dependence of the phase correlation. The model suite provides a new tool for investigating process and/or parameter dependence of observed random internal tides, and for identifying their important sources.

1 Introduction

Internal tides are known to contain a substantial component that cannot be explained by harmonic analysis (based on the superposition of sinusoids at tidal frequencies with constant amplitudes and phases). The remaining nonharmonic component is
25 considered to be caused by the random variability of stratification and background currents. For nonharmonic internal tides originating from distributed sources, the major difficulties for understanding the physics include the following two factors: (i) statistical principles tend to make the observed variability insensitive to the underlying physical processes, and (ii) observed nonharmonic internal tides often consist of many waves propagating towards different directions with different degrees of randomness. To tackle the problem (ii) considering the difficulty (i), this study develops a new framework for process-based
30 modelling of nonharmonic internal tides observed at a fixed location by combining adjoint, statistical, and stochastic approaches, and uses its implementation to investigate important processes and parameters controlling nonharmonic internal-tide variance.

   Internal tides are internal waves with tidal frequencies, primarily in the diurnal (≈24 h period) and semidiurnal (≈12 h period) bands. They have different vertical structures, or modes, and lower modes have larger propagation speeds and usually
35 larger energies. (The internal-tide modes are referred to as "baroclinic" modes to distinguish them from the usual tides, or the "barotropic" mode. It is customary to count the first baroclinic mode as vertical mode one, or VM1.) Internal tides are generated by the interaction of tidal currents with topographic slopes, which implies their coherence with the tide-generating forces at the generation sites. However, they gradually become incoherent (or non-phase-locked) as they propagate away from the generation sites (e.g., Rainville and Pinkel, 2006; Buijsman et al., 2017; Alford et al., 2019). This process is considered to be
40 caused primarily by phase modulation through the variability of the wave propagation speed (Rainville and Pinkel, 2006; Park and Watts, 2006), which is in turn caused by temporally and spatially varying pycnocline heaving and advection (Buijsman et al., 2017; Zaron and Egbert, 2014). Although the variability of internal-tide generation can be substantial (Kerry et al., 2016), the amplitude modulation is overall considered to be less important than the phase modulation (Zaron and Egbert, 2014; Colosi and Munk, 2006).

45 Part I of this study (Shimizu, Companion Paper, hereafter referred to as Part I) developed a statistical model of nonharmonic internal tides, which is the basis of the modelling framework proposed in this study. (Following Part I, the term "nonharmonic" internal tide is used for the random component of internal tides, which is also referred to as "incoherent"," nonstationary", or "non-phase-locked" internal tides in previous studies.) The statistical model approximates nonharmonic internal tides observed at a fixed location as the superposition of sinusoidal waves from an arbitrary number of independent sources. The model shows
50 that (i) the envelope-amplitude distribution approaches a universal form given by a generalization of the Rayleigh distribution when the number of independent wave sources is sufficiently large (or when the central limit theorem in statistics is applicable), and (ii) this is likely to require only 3 to 10 independent sources in realistic oceanic conditions. The comparisons of model and observed probability density functions (PDFs) showed the applicability of the limiting distribution to vertical-mode-one (VM1) to vertical-mode-four (VM4) internal tides in the diurnal, semidiurnal, and quarterdiurnal (≈6 h period) frequency bands on a
55 continental shelf, provided that the spectra showed the corresponding tidal peaks clearly. When nonharmonic internal tides are

in the "many source" limit, one of the most important questions is what determines the variance, which controls the PDFs (and the associated higher-order statistics).

The above statistical study is an important step forward; however, it also suggests difficulty in investigating the physical processes of nonharmonic internal tides based on their variability at an observation location. This is because the PDFs tend to approach the universal form by statistical principles, regardless of the details of individual wave components. For example, the phase of observed nonharmonic internal tides can be nearly uniformly distributed when the phases of individual wave components vary less than 5% (of the total 2π), and the observed amplitude tends to show large variability when the amplitudes of individual components do not vary at all. Furthermore, nonharmonic internal tides often result from the superposition of many waves propagating towards different directions with different degrees of randomness. So, even when complete spatial and temporal information are available, for example, from the outputs of hydrodynamic modelling, it is often not straightforward to identify wave components from a particular source region or a particular process. It appears that process-based studies are most straightforward when internal tides originate from a localized source or a small number of adjacent sources, so that the evolution of internal tides can be analysed based on the distance (or travel time) from the source(s) without interference. Using hydrodynamic modelling, such studies have been done in regions around Hawaii and French Polynesian Islands (Zaron and Egbert, 2014; Buijsman et al., 2017). However, this approach is applicable only to a small fraction of the world ocean, and not suitable for regions affected by distributed sources, including continental shelves facing open ocean. In addition, although comprehensive literature survey is difficult, the methodologies developed for wave propagation in random media in other fields of physics and engineering do not appear to be directly applicable to distributed sources, because they usually consider a signal from a small number of point sources (e.g., Colosi, 2016, for underwater acoustics).

An alternative approach for process-based studies with wider applicability is a kind of inverse modelling of internal tides observed at a fixed location. By limiting the locations of interest, the adjoint of a hydrodynamic model can be used to trace internal tides arriving at a fixed observation location back to the distributed sources (Shimizu, 2024a). This information in turn enables assignment of different degrees of randomness to waves arriving from different sources. If the degrees of randomness are calculated based on process understanding, it would be possible to calculate nonharmonic internal-tide variance, compare it with observations, and investigate the dependence of the modelled variance on different processes and/or parameters. This "inverse" approach would also provide useful information such as the map of nonharmonic internal-tide sources and integrated regional contributions. This type of modelling can be viewed not only as an inverse approach but also a "synthesis" approach, because the model can be built up from process understanding, and the results can be used to check whether the current understanding "adds up" to explain the observed variance.

This study aims to develop a new framework for process-based modelling of nonharmonic internal tides by combining the statistical model from Part I with adjoint and stochastic models, and then to use its implementation to investigate processes and parameters controlling nonharmonic internal-tide variance. As an example application, the resultant model suite is applied to VM1 semidiurnal internal tides observed at a mooring site on the Australian North West Shelf, and the results are compared to the observed variance and PDF. Since this is the first application of the proposed modelling framework, the application is
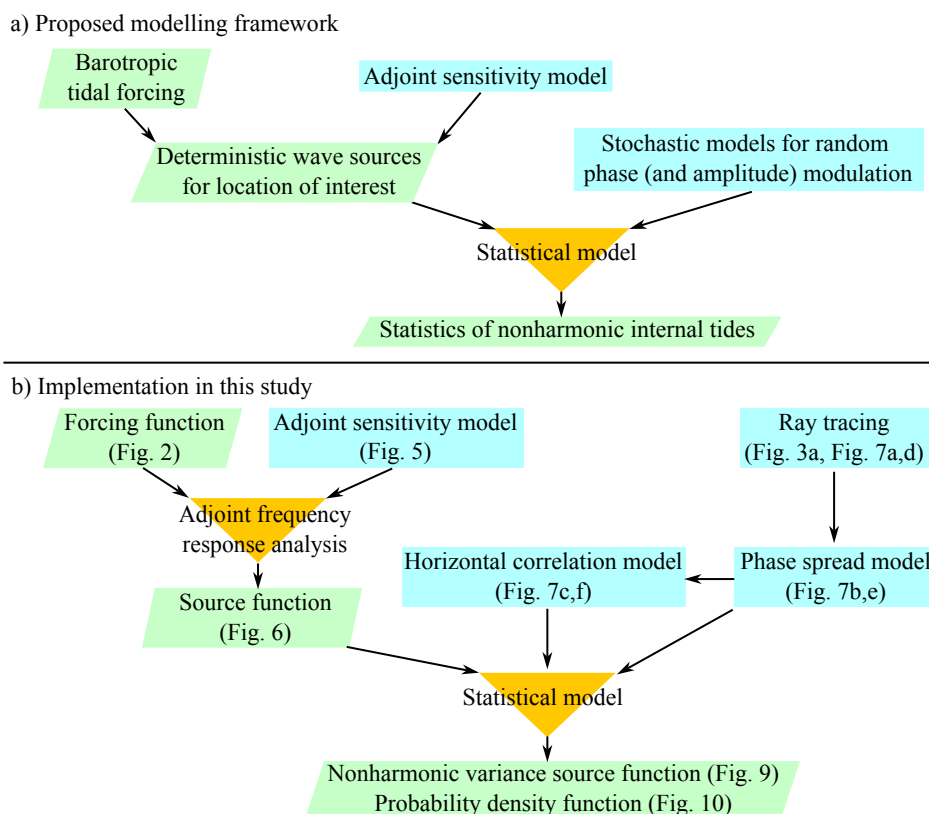
Figure 1. Overview of proposed modelling framework and its implementation in this study.

90 intended to be a feasibility test. The models are intentionally simplified, and used to understand the dependence of modelled variance on the model parameters, rather than attempting to provide a single best estimate.

This paper is organized as follows. Section 2 presents an overview of the proposed modelling framework and model suite, and Section 3 presents the theoretical background of individual model components, including a short summary of the statistical model developed in Part I. Section 4 presents methodology, particularly the details of numerical methods. The results of an

95 example application to the Australian North West Shelf are shown in Section 5, followed by discussion in Section 6. This paper ends with a list of conclusions in Section 7.

2   Modelling framework and its implementation

An overview of the proposed modelling framework is shown in Fig. 1a. The key component is the statistical model developed in Part I. It calculates the statistics of nonharmonic internal tides by randomizing the phases (and optionally amplitudes)

100 of individual internal-tide components arriving at an observation location from deterministic sources using the statistics of random phase modulation. For distributed internal-tide sources in realistic oceanic applications, the horizontal distributions of

the sources and phase statistics are necessary. The source distribution can be modelled using an adjoint sensitivity model and barotropic tidal forcing. Currently, there appears to be no standard method to model the distributions of phase statistics. Since phase statistics vary with wave propagation (i.e., nonstationary), its process-based modelling appears to require a stochastic approach. In addition to random variability of the wave phases, the horizontal correlation of phase modulation is necessary because it introduces the correlation of waves arriving from individual sources, but the statistical model assumes independent waves. So, this study proposes the modelling framework shown in Fig. 1a, whose detailed implementation can evolve in the future.

An overview of the implementation of the modelling framework in this study is shown in Fig. 1b. Apart from the statistical model, another key component is a new method referred to as "adjoint frequency response analysis", which is a combination of numerical adjoint sensitivity modelling and the frequency response analysis from Fourier theory. The output is the horizontally distributed deterministic sources of internal tides observed at a fixed location, which is referred to as the "source function" in this study. Stochastic models are separately developed to model the phase spread and the horizontal (two-dimensional) correlation of phase modulation, both of which are assumed to be caused by random variability of phase speed. The results of these models provide two input parameters of the statistical model: the strengths of independent sources and the phase spread of waves arriving from individual sources. One of the important model outputs is the horizontal source distribution of nonharmonic internal-tide variance, which is referred to as the "nonharmonic variance source function" in this study. In turn, this can be used to calculate the PDF of nonharmonic internal-tide amplitude, and the contributions of different source regions to the variance.

The entire process in Fig. 1b can be viewed as applying two model-derived filters to the global and deterministic "forcing function" from the barotropic mode to individual baroclinic modes: the first filter transforms the forcing function to the source function relevant only to a particular observation location, and the second filter transforms the deterministic source function to the nonharmonic variance source function relevant only to the random component of internal tides (green boxes in Fig. 1b).

3 Theoretical background

3.1 Statistical model

The basis of the modelling framework proposed in this paper is the statistical model developed in Part I. Only a fraction of the model is needed in the majority of Part II, which primarily considers the variance of nonharmonic internal tides. This section introduces relevant relationships from Part I for independent waves, and then extends them to correlated waves. The method for calculating probability density function (PDF), which is used only briefly near the end of this paper, is described in Part I.

We first introduce relevant relationships from Part I. The statistical model in Part I considers internal tides with a single vertical-mode structure in a narrow frequency band observed at a fixed observation location, and approximates them as a sinusoidal time series that has the deterministic angular frequency ω, a random amplitude A, and a random phase lag Θ. Furthermore, it is assumed that this signal results from the superposition of independent and non-identically distributed N sinusoidal wave components, each of which has a random amplitude A_j and a random phase lag Θ_j. Then, the signal can be

135 expressed as

$$Ae^{-\mathrm{i}\Theta}e^{\mathrm{i}\omega t} = \sum_{j=1}^{N} A_j e^{-\mathrm{i}\Theta_j} e^{\mathrm{i}\omega t}, \tag{1}$$

where t is time. Unlike Part I, only deterministic amplitudes $A_j = a_j$ are considered for individual wave components. The phase PDF is assumed to be the wrapped normal (or Gaussian) distribution as in Part I:

$$f_{\Theta_j}(\theta_j) = \frac{1}{\sqrt{2\pi}\sigma_j} \sum_{k=-\infty}^{\infty} \exp\left(-\frac{(\theta_j - \varphi_j + 2\pi k)^2}{2\sigma_j^2}\right), \tag{2}$$

140 where φ_j is the phase lag, and σ_j is the standard deviation of the phase (short-hand notation for σ_{Θ_j}). The wrapped normal distribution is a circular analogue of the Gaussian distribution, and defined for any one period of 2π. It approaches the Gaussian distribution in the limit $\sigma_j \to 0$, but approaches the uniform distribution in the limit $\sigma_j \to \infty$. Since harmonic analysis determines harmonic amplitudes and phase lags using the method of least squares, the complex-valued amplitudes are further decomposed into the expected values and deviations from them:

145 $$Ae^{-\mathrm{i}\Theta} = re^{-\mathrm{i}\varphi} + A'e^{-\mathrm{i}\varphi}e^{-\mathrm{i}\Theta'}$$

$$= \sum_{j=1}^{N} \left(r_j e^{-\mathrm{i}\varphi_j} + A'_j e^{-\mathrm{i}\varphi_j} e^{-\mathrm{i}\Theta'_j}\right). \tag{3}$$

Here, r and φ are the amplitude and phase lag of the expected complex-valued amplitude on the complex plane, and A' and Θ' are the amplitude and phase lag of the deviation. Note that (r, φ) and (A', Θ') correspond to harmonic and nonharmonic internal tides, respectively. Note also that the definition of Θ' has been changed slightly from Part I. Assuming tentatively that

150 σ_j in Eq. (2) are known, and that all the wave components are independent, the expectation and variance of the complex-valued random amplitudes $A_j e^{-\mathrm{i}\Theta_j}$ are

$$\mathrm{E}\left(A_j e^{-\mathrm{i}\Theta_j}\right) = r_j e^{-\mathrm{i}\varphi_j} = a_j \mu_j e^{-\mathrm{i}\varphi_j}, \tag{4a}$$

$$\mathrm{Var}\left(A_j e^{-\mathrm{i}\Theta_j}\right) = \mathrm{E}\left(A_j'^2\right) = a_j^2 \varsigma_j^2, \tag{4b}$$

$$\mu_j = e^{-\sigma_j^2/2}, \tag{4c}$$

155 $$\varsigma_j^2 = 1 - e^{-\sigma_j^2}. \tag{4d}$$

Hereafter, $\mathrm{E}(\cdot)$ and $\mathrm{Var}(\cdot)$ denote the expected value and variance, respectively. For complex-valued variables, the variance is defined as $\mathrm{Var}(X) = \mathrm{E}((X - \mathrm{E}(X))(X - \mathrm{E}(X))^*)$. Hereafter, the superscript $*$ denotes complex conjugate. Then, because of the independence of individual wave components, $\mathrm{E}\left(A'^2\right)$ is given by (see Part I for justification):

$$\mathrm{E}\left(A'^2\right) = \sum_{j=1}^{N} \mathrm{E}\left(A_j'^2\right). \tag{5}$$

160 Note that $\mathrm{E}\left(A'^2\right)$ is the variance of the envelope amplitude of nonharmonic internal tides, and is twice the nonharmonic internal-tide variance because the sinusoidal "carrier" wave (i.e., $e^{\mathrm{i}\omega t}$ in Eq. (1)) has the variance of 1/2. As previously shown

by Colosi and Munk (2006), the phase spread σ_j is an important parameter that separates the total variance into harmonic and nonharmonic parts.

165   The above argument assumes the independence of individual wave components; however, the horizontal correlation of phase modulation along the propagation paths introduces the correlation of wave components arriving from individual sources. To consider the horizontal correlation, we remove the assumption of independent wave components in Eqs. (1) and (3), and calculate the covariance of the ith and j^{th} wave components. Using $A_j = a_j$ and Eq. (4b), we get

$$\text{Cov}\left(A_i' e^{-\mathrm{i}\varphi_i} e^{-\mathrm{i}\Theta_i'}, A_j' e^{-\mathrm{i}\varphi_j} e^{-\mathrm{i}\Theta_j'}\right) = s_i \varsigma_i R_{ij} \varsigma_j s_j^*, \tag{6}$$

where $s_j = a_j e^{-\mathrm{i}\varphi_j}$ are complex-valued pre-modulation wave amplitudes from individual sources (hereafter referred to as
170   "sources"), $R_{ij} = \text{Cov}\left(e^{-\mathrm{i}\Theta_i'}, e^{-\mathrm{i}\Theta_j'}\right)$, and the covariance is defined as $\text{Cov}(X,Y) = \text{E}((X - \text{E}(X))(Y - \text{E}(Y))^*)$. Note that Θ_j' do not follow the wrapped normal distribution, Eq. (2), but $e^{-\mathrm{i}\Theta_j'}$ can be expressed in terms of $e^{-\mathrm{i}\Theta_j}$, μ_j, and ς_j using Eqs. (3) and (4). This yields

$$R_{ij} = \frac{1}{\varsigma_i \varsigma_j}\left(\exp\left\{-\frac{1}{2}\text{E}\left(\Delta\Theta''^2\right)\right\} - \mu_i \mu_j\right), \tag{7}$$

where $\Delta\Theta'' = \Theta_i'' - \Theta_j''$. The new phase variables $\Theta_j'' = \Theta_j - \varphi_j$ are wrapped-normal variables with zero mean phase. Since
175   the difference of correlated wrapped-normal variables is a wrapped-normal variable, the expectation in the above equation is obtained using

$$\text{E}\left(e^{-\mathrm{i}\Delta\Theta''}\right) = \exp\left\{-\frac{1}{2}\text{E}\left(\Delta\Theta''^2\right)\right\}, \tag{8}$$

which is the same relationship as for normally distributed phase, derived previously by Colosi and Munk (2006) and Geoffroy and Nycander (2022). To proceed, these studies assumed the correlation functions of Θ_i'' and Θ_j'', but we aim to express the
180   above expectation as a function of the variance and correlation length of phase speed. This is done by stochastic modelling, as described in Section 3.5.

    The correlation coefficients, Eq. (7), can be used to convert correlated sources (e.g., from hydrodynamic modelling) to effectively independent sources that can be used in the statistical model. To do so, we write the complex-valued amplitude of nonharmonic internal tides $A' e^{-\mathrm{i}\varphi} e^{-\mathrm{i}\Theta'}$ in two ways. On the one hand, we assume that the waves from individual sources
185    $s_j = a_j e^{-\mathrm{i}\varphi_j}$ are later modulated by horizontally correlated random phase shifts, yielding

$$A' e^{-\mathrm{i}\varphi} e^{-\mathrm{i}\Theta'} = \boldsymbol{s}_{\text{phys}}^T \boldsymbol{\Sigma} \boldsymbol{n}_{\text{corr}}. \tag{9}$$

Here, $\boldsymbol{s}$ is the vector containing s_j, and $\boldsymbol{\Sigma}$ is a diagonal matrix whose diagonal components are ς_j defined in Eq. (4d). Hereafter, the superscript T denotes transpose. The above form is chosen so that the vector $\boldsymbol{n}$, with its components $\varsigma_j^{-1}\left(e^{-\mathrm{i}\Theta_j''} - \text{E}\left(e^{-\mathrm{i}\Theta_j''}\right)\right)$, is a vector containing random variables with zero mean and unit variance (but not Gaussian) on the complex plane. The sub-
190   script "phys" emphasizes that the variable is calculated based on physics (in this study, by the adjoint frequency response analysis introduced in the next section), and the subscript "corr" emphasizes horizontally correlated random variables. The

statistical model, on the other hand, requires independent random variables:

$$A'e^{-\mathrm{i}\varphi}e^{-\mathrm{i}\Theta'} = \boldsymbol{s}_{\mathrm{stat}}^T \boldsymbol{\Sigma}\boldsymbol{n}, \tag{10}$$

where the vector $\boldsymbol{s}_{\mathrm{stat}}$ contains the amplitudes of independent sources. Now, we may assume that two random vectors are related as $\boldsymbol{n}_{\mathrm{corr}} = \mathbf{R}^{1/2}\boldsymbol{n}$, where $\mathbf{R} = \mathbf{R}^{1/2}\mathbf{R}^{T/2}$ is the horizontal correlation coefficient matrix whose components are given by Eq. (7). Assuming tentatively that $\mathbf{R}^{1/2}$ is known, the comparison of the above two equations shows

$$\boldsymbol{s}_{\mathrm{stat}} = \boldsymbol{\Sigma}^{-1}\mathbf{R}^{T/2}\boldsymbol{\Sigma}\boldsymbol{s}_{\mathrm{phys}}. \tag{11}$$

We use this relationship to convert horizontally correlated sources calculated based on physics to effectively independent sources that can be used in the statistical model. Then, considering Eqs. (4b) and (5) in a matrix form, twice the nonharmonic internal-tide variance $\mathrm{E}\left(A'^2\right)$ can be written as

$$\begin{aligned}\mathrm{E}\left(A'^2\right) &= \boldsymbol{s}_{\mathrm{stat}}^H \boldsymbol{\Sigma}^2 \boldsymbol{s}_{\mathrm{stat}} \\ &= \boldsymbol{s}_{\mathrm{phys}}^H \boldsymbol{\Sigma}\mathbf{R}\boldsymbol{\Sigma}\boldsymbol{s}_{\mathrm{phys}}.\end{aligned} \tag{12}$$

Hereafter, the superscript H denotes conjugate transpose. Note that the (i,j) component in the summation corresponds to Eq. (6).

Before proceeding further, it is worth noting three detailed points regarding the above treatment of horizontal correlation.

The first point is that $\mathbf{R}^{1/2}$ is not unique for the same $\mathbf{R}$. For example, if sources at two locations are perfectly correlated with zero harmonic phase lag, the same amplitude a_0, and the same coefficient of variation ς_0, $\mathbf{R}$ is a matrix with all the elements being unity. The Cholesky decomposition, a common numerical method to calculate $\mathbf{R}^{1/2}$, yields

$$\mathbf{R}^{1/2} = \begin{bmatrix} 1 & 0 \\ 1 & 0 \end{bmatrix}. \tag{13}$$

Then, $\boldsymbol{s}_{\mathrm{stat}} = [2a_0\ 0]^T$. This is reasonable in that statistically independent sources consist of a single source whose amplitude is the sum of those of two perfectly correlated sources. But it also has a problem that the ordering of vector elements in $\boldsymbol{s}$ determines where this single source is located. An alternative choice of $\mathbf{R}^{1/2}$ is

$$\mathbf{R}^{1/2} = \frac{1}{\sqrt{2}} \begin{bmatrix} 1 & 1 \\ 1 & 1 \end{bmatrix}. \tag{14}$$

In this case, $\boldsymbol{s}_{\mathrm{stat}} = [\sqrt{2}a_0\ \sqrt{2}a_0]^T$. It is not intuitive to have two supposedly independent sources for two perfectly correlated sources. However, it has an advantage that the result does not depend on the ordering of vector elements in $\boldsymbol{s}$, and there is a numerical method to calculate this type of $\mathbf{R}^{1/2}$ much more efficiently than the Cholesky decomposition for large problems. Importantly, in both cases, $\mathrm{E}\left(A'^2\right) = 4a_0^2\varsigma_0^2$ from Eq. (12), because $\mathbf{R} = \mathbf{R}^{1/2}\mathbf{R}^{T/2}$ is the same. These examples suggest that $\boldsymbol{s}_{\mathrm{stat}}$ provides effectively independent sources that can be used in the statistical model to calculate nonharmonic internal-tide variance, but the horizontal distribution of the independent sources is uncertain within the correlation length of phase modulation.

The second point is that the horizontal phase correlation has a large impact on nonharmonic internal-tide variance. As a simple example, consider waves arriving from N grid points with the same amplitude a_0 and coefficient of variation ς_0 in a numerical hydrodynamic model. In the absence of horizontal correlation ($\mathbf{R} = \mathbf{I}$), the variance is $N a_0^2 \varsigma_0^2$ from Eq. (12). If the waves are perfectly correlated, $\mathbf{R}$ is a matrix with all the elements being unity. Then, the variance is $N^2 a_0^2 \varsigma_0^2$. Considering one source region resolved by N grid points, this shows that the horizontal correlation has to be considered for gridded sources, otherwise the results would be highly dependent on grid resolution. Physically, this also suggests that the horizontal extent of source regions can be an important factor controlling nonharmonic internal-tide variance.

The third point is that, strictly speaking, the above treatment of horizontal correlation cannot be used to investigate the details of the PDF or higher moments, because the statistical model uses a non-Gaussian distribution on the complex plane for individual wave components. However, the above method works in the limit of many independent sources (or when the central limit theorem is applicable), because the limiting distribution is determined by the (co)variance of the joint Gaussian distribution on the complex plane, which can be calculated, for example, based on Eq. (5), regardless of the PDF of individual sources. The results of Part I suggest that this "many source" limit would be common for internal tides.

The above statistical model suggests that process-based modelling of nonharmonic internal tides is possible if process-based models of the deterministic internal-tide sources (or pre-modulation amplitudes) $s_j = a_j e^{-\mathrm{i}\varphi_j}$, the phase variance σ_j^2, and the variance of horizontal phase difference $\mathrm{E}\left(\Delta\Theta''^2\right)$ are available. These three models are developed in turn in the following sections.

3.2 Adjoint sensitivity model and adjoint frequency response analysis

In order to calculate the deterministic sources of internal tides for a fixed observation location, we use a combination of adjoint sensitivity modelling and the frequency response analysis from Fourier theory. To introduce the method, let us start from a quick overview of the adjoint method, which is often used in the so-called four-dimensional variational data assimilation (e.g., Bennett, 2002; Wunsch, 2006).

The adjoint method is based on a so-called forward model and an objective (or cost) function. We consider a spatially-discretized linear numerical hydrodynamic model:

$$\frac{\partial \boldsymbol{x}}{\partial t} = -\mathbf{L}\boldsymbol{x} + \boldsymbol{f}, \tag{15}$$

where $\boldsymbol{x}(t)$ is the model state vector containing the model's prognostic variables at all the grid points, $\mathbf{L}$ is the matrix operator representing the linear dynamics, and $\boldsymbol{f}$ is the external forcing. For the purpose of describing theoretical background, the model is assumed to be formulated for a single baroclinic mode forced by barotropic tides, so that the equations have a form analogous to the shallow water equations for a homogeneous fluid (Shimizu, 2011, 2017, 2019). Since the model is linear, the solution can be written as

$$\boldsymbol{x}(t) = \int\limits_{-\infty}^{t} \mathbf{H}(t - \tau)\boldsymbol{f}(\tau)d\tau, \tag{16}$$

where each column of the matrix $\mathbf{H}$ contains the impulse response function. Using the model solution, we consider a linear objective function $J = \boldsymbol{w}^H \boldsymbol{x}$, tentatively defined at a particular time t_j. The variable $\boldsymbol{w}$ is the weight vector used to define J. There are various expressions for J:

$$J(t_j) = \boldsymbol{w}^H \boldsymbol{x}(t_j) \tag{17a}$$

$$= \boldsymbol{w}^H \int_{-\infty}^{t_j} \mathbf{H}(t_j - \tau) \boldsymbol{f}(\tau) d\tau \tag{17b}$$

$$= \int_{-\infty}^{t_j} \left(\mathbf{H}^H(t_j - \tau) \boldsymbol{w} \right)^H \boldsymbol{f}(\tau) d\tau \tag{17c}$$

$$= \int_{-\infty}^{t_j} \boldsymbol{\lambda}^H(t_j - \tau) \boldsymbol{f}(\tau) d\tau. \tag{17d}$$

This manipulation is equivalent to the linear and continuous version of the derivation by Marotzke et al. (1999). The variable $\boldsymbol{\lambda}$ is so-called adjoint sensitivity, or the sensitivity of J to $\boldsymbol{x}$. It can be calculated from the adjoint model associated with Eqs. (15) and (17a):

$$-\frac{\partial \boldsymbol{\lambda}}{\partial t} = -\mathbf{L}^H \boldsymbol{\lambda}, \tag{18a}$$

$$\boldsymbol{\lambda} = \boldsymbol{w} \quad \text{at} \quad t = t_j. \tag{18b}$$

The above differential equations are integrated backwards in time from the "initial" condition given at $t = t_j$.

For periodic or oscillatory problems, it is often convenient to consider the above problems in the frequency domain. Since Eq. (16) is convolution in time, the convolution theorem in Fourier theory shows that its Fourier transform is

$$\tilde{\boldsymbol{x}}(\omega) = \tilde{\mathbf{H}}(\omega) \tilde{\boldsymbol{f}}(\omega), \tag{19}$$

where $\tilde{\mathbf{H}}$ contains the frequency response function. Hereafter, tilde is used for Fourier-transformed variables. If we now allow t_j to vary and consider time-dependent J (but with time-independent $\boldsymbol{w}$), a similar method can be used for J, because Eq. (17d) in the frequency domain is

$$\tilde{J}(\omega) = \tilde{\boldsymbol{\lambda}}(\omega)^H \tilde{\boldsymbol{f}}(\omega). \tag{20}$$

In this study, $\tilde{\boldsymbol{\lambda}}$ is referred to as the "adjoint frequency response function", and analysis based on the above relationship as "adjoint frequency response analysis". Although $\tilde{J}$ can also be calculated as $\boldsymbol{w}^H \tilde{\boldsymbol{x}}$, the adjoint frequency response function has an important advantage in this study, which becomes clear later.

In the above derivation, the time-dependent adjoint model Eq. (18) and Fourier transform are used to calculate $\tilde{\boldsymbol{\lambda}}$; however, it is more straightforward to calculate $\tilde{\boldsymbol{\lambda}}$ by assuming a periodic solution from the beginning. Assuming $\boldsymbol{x} = \tilde{\boldsymbol{x}} e^{\mathrm{i}\omega t}$ and $\boldsymbol{f} = \tilde{\boldsymbol{f}} e^{\mathrm{i}\omega t}$ in Eq. (15), it follows that the corresponding adjoint model is

$$-\mathrm{i}\omega \tilde{\boldsymbol{\lambda}} = -\mathbf{L}^H \tilde{\boldsymbol{\lambda}} + \boldsymbol{w}. \tag{21}$$
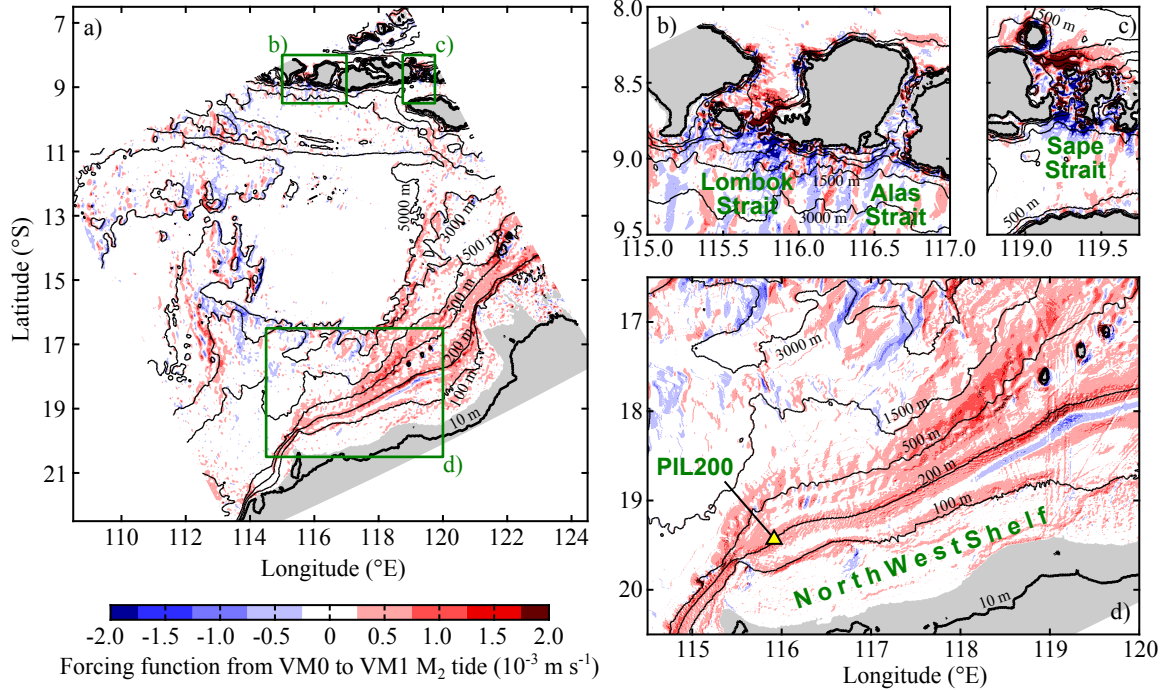
Figure 2. Forcing function from barotropic-mode (VM0) to vertical-mode-one (VM1) M_2 tide (at zero Greenwich phase lag). It corresponds to $\tilde{f}$ in Eq. (23). Panels (b-d) show zoomed views of green boxes in (a). Grey shading shows regions where VM1 celerity is less than $0.1\,\mathrm{m\,s^{-1}}$.

To apply the adjoint frequency response analysis to single-vertical-mode internal tides observed at a fixed location, we use the vertical-mode amplitude of isopycnal displacement as the objective function, and use the model formulation based on vertical-mode decomposition in Shimizu (2011) and Shimizu (2019). The formulation employs horizontally varying vertical modes that are calculated using local water depths and stratification, in order to include the effects of steep slopes (for linear waves). More details are described in Appendix A. An advantage of this formulation is that it yields the evolutionary equations of the form Eq. (15) with explicit forcing function from barotropic tides to individual baroclinic modes, which depends on barotropic tidal currents, bottom slope, and vertical-mode structure. As an example, the forcing function from barotropic to VM1 M_2 tide is shown in Fig. 2.

It is convenient to write Eq. (20) in different ways for later purposes. The equation can be written as

$$2\tilde{J} = \sum_{j=1}^{N} s_j = \sum_{j=1}^{N} a_j e^{-\mathrm{i}\varphi_j}, \tag{22}$$

where s_j is twice the jth component of the vector sum on the right-hand-side of Eq. (20), and the subscript j is a horizontal grid index that indicates the value at horizontal location $\overrightarrow{x}_j$ (assuming only one vertical mode in the model). The variable $s_j = a_j e^{-\mathrm{i}\varphi_j}$ is sought-after wave sources corresponding to s_{phys} in Eq. (11). The factor 2 is multiplied to $\tilde{J}$ because the use of

the convolution theorem requires $\tilde{J}$ to be two-sided (ω in Eq. (20) can be positive or negative), but harmonic analysis and the statistical model assume one-sided spectra (positive ω only).

If only one vertical mode is considered in the hydrodynamic model, Eq. (20) can also be written in a continuous form as

$$2\tilde{J} = \int s(\overrightarrow{x})d\overrightarrow{x} = \int 2\tilde{\lambda}^*(\overrightarrow{x})\tilde{f}(\overrightarrow{x})d\overrightarrow{x}, \qquad (23)$$

where s, $\tilde{\lambda}$, and $\tilde{f}$ are the continuous versions of $\boldsymbol{s}$, $\tilde{\boldsymbol{\lambda}}$, and $\tilde{\boldsymbol{f}}$, respectively. The function $s(\overrightarrow{x})$ is hereafter referred to as the "source function" (more correctly, source density function). The middle expression shows that, because the horizontal integral of the source function yields $2\tilde{J}$, s can be mapped to identify important source regions. Also, a regional integral of s yields the contribution of that region to the total $2\tilde{J}$. The right expression shows that the adjoint frequency response function $\tilde{\lambda}$ acts as a transfer function from the forcing function $\tilde{f}$, which provides forcing in a global sense, to the source function s, which provides forcing relevant to a specific variable at an observation location (where $\boldsymbol{w}$ is nonzero). The maps of $\tilde{f}$ and $\tilde{\lambda}$ can be used to identify regions where forcing and dynamic response are large. The important advantage of the source function in this study is that it provides horizontally distributed sources of internal tides observed at a fixed location, so that different phase statistics can be assigned to different (for example, local and remote) sources. If the model includes multiple vertical modes, the maps of $\tilde{f}$, $\tilde{\lambda}$, and s can be produced for individual modes, and the total $2\tilde{J}$ is given by the sum over all available modes.

Applying the same reasoning to Eq. (12) divided by 2, the continuous version of Eq. (12) can be written as

$$\frac{1}{2}\mathrm{E}\left(A'^2\right) = \int s_{nh}(\overrightarrow{x})d\overrightarrow{x}$$
$$= \int\int \frac{1}{2}s(\overrightarrow{x}_1)\varsigma(\overrightarrow{x}_1)R(\overrightarrow{x}_1,\overrightarrow{x}_2)\varsigma(\overrightarrow{x}_2)s(\overrightarrow{x}_2)d\overrightarrow{x}_1 d\overrightarrow{x}_2. \qquad (24)$$

The variable s_{nh} is referred to as the "nonharmonic variance source function" in this study. It can also be mapped or regionally integrated. However, unlike the source function, s_{nh} is not unique within the correlation length of phase modulation, as explained in Section 3.1.

3.3 Covariance equations for stochastic variables

In order to model phase variance σ_j^2 and the variance of horizontal phase difference $\mathrm{E}\left(\Delta\Theta''^2\right)$, we develop linear stochastic models in the following sections. To do so, it is convenient to use general relationships for stochastic differential equations (Särkkä and Solin, 2019), and a brief summary is provided here.

Let us consider linear simultaneous stochastic differential equations

$$d\boldsymbol{x} = \mathbf{A}\boldsymbol{x}dt + \mathbf{B}d\boldsymbol{b}, \qquad (25)$$

where $\boldsymbol{x}(t)$ is a vector containing the model prognostic variables. The vector $\boldsymbol{b}(t)$ contains so-called Brownian motion (see e.g., Särkkä and Solin, 2019, chap. 4.1). The increment $d\boldsymbol{b}$ is a vector containing white Gaussian noise with zero mean and the covariance $\mathrm{E}\left(d\boldsymbol{b}d\boldsymbol{b}^T\right) = \mathbf{Q}dt$, where $\mathbf{Q}$ is the so-called "diffusion coefficient" matrix of the Brownian process. Intuitively, the above equations can be formally divided by dt and $d\boldsymbol{b}/dt$ regarded as a vector containing white noise, although this view
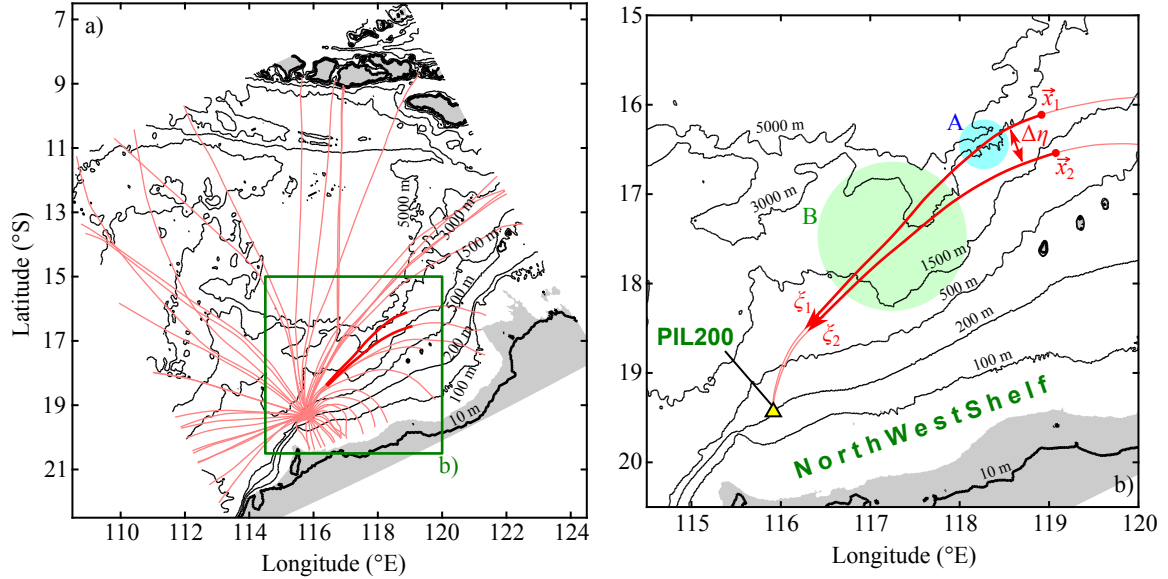
Figure 3. An example of ray paths for vertical-mode-one (VM1) M₂ internal tide and schematics of variables used in cross-path phase difference modelling. Pink lines indicate ray paths. Panel (b) shows zoomed view of green box in (a) for two example ray paths. Green and blue circles indicate hypothetical regions of random phase-speed variability caused by eddies. Grey shading shows regions where VM1 celerity is less than $0.1\ \mathrm{m\,s^{-1}}$.

is mathematically incorrect in general. The matrices $\mathbf{A}$ and $\mathbf{B}$ may depend on t, but not on $\boldsymbol{x}$ in linear stochastic differential equations. The matrix $\mathbf{Q}$ is independent of t and $\boldsymbol{x}$.

The covariance equations associated with Eq. (25) are (Särkkä and Solin, 2019, chap. 6.1)

$$\frac{d\mathbf{P}}{dt} = \mathbf{A}\mathbf{P} + \mathbf{P}\mathbf{A}^T + \mathbf{B}\mathbf{Q}\mathbf{B}^T, \tag{26}$$

where $\mathbf{P}(t) = \mathrm{E}\left((\boldsymbol{x} - \mathrm{E}(\boldsymbol{x}))(\boldsymbol{x} - \mathrm{E}(\boldsymbol{x}))^T\right)$ is the covariance matrix. Note that we need to integrate only the above ordinary differential equations in this study, although the formulation is based on stochastic differential equations, Eq. (25). Hereafter, the components of $\mathbf{P}$ and $\mathbf{Q}$ are denoted by two subscripts corresponding to prognostic variables. For example, if one of the components in $\boldsymbol{x}$ is the phase speed c, then $P_{cc} = \sigma_C^2$ is the phase-speed variance.

3.4 Stochastic phase spread model

We now consider the calculation of the phase variance σ_j^2 in Eq. (4). Following Zaron and Egbert (2014), σ_j^2 can be calculated considering the variation of the wave phase θ and the phase speed c in the phase relationship $d\theta = \omega(dt - c^{-1}d\xi)$, where ξ is the coordinate along the wave propagation path. Some examples of wave propagation paths are shown in Fig. 3a. To introduce random components in θ and c, we write $\theta = \overline{\theta} + \theta''$ and $c = \overline{c} + c'$, where $\overline{\theta}$ and $\overline{c}$ are the respective mean components, and θ'' and c' are the respective stochastic components with zero mean. Assuming $|c'| \ll \overline{c}$, the relationship between θ'' and c' from

the phase relationship is

$$d\theta'' \sim \frac{\omega c'}{\overline{c}^2} d\xi \sim \frac{\omega c'}{\overline{c}} dt. \tag{27}$$

Although we consider spatial integration, the independent variable is changed from ξ to t in the right expression. This is partly because time is usually used as the independent variable in stochastic differential equations, and partly because it is more

340   convenient to use the same independent variable as in standard ray tracing, which is used to calculate wave propagation paths (described in Section 4.3).

     Since θ'' and c' are stochastic variables, Eq. (27) is a stochastic differential equation. Stochastic differential equations are commonly forced by white Gaussian noise, but it is undesirable to assume c' as white noise because c' certainly has spatial correlation. A common "trick" used to deal with correlated noise is to introduce an additional stochastic equation driven by white noise which yields the desired correlation function (see e.g., Särkkä and Solin, 2019, chap. 12.3). In our case, we assume

345   that c' follows

$$dc' = -\frac{\overline{c}}{L_C} c' dt + \sqrt{\frac{\overline{c}}{L_C}} db, \tag{28}$$

where L_C is the e-folding correlation length of c'. The "diffusion coefficient" Q_{cc} of the Brownian motion b is unknown at this stage, but determined shortly. Assuming that $\overline{c}$ and L_C remain locally constant, the above equation implies that the power

350   spectrum of c' is Lorentzian, and the (along-path) correlation function is (Särkkä and Solin, 2019, chap. 6.5)

$$R_c = e^{-\overline{c}|\Delta t|/L_C} \sim e^{-|\Delta \xi|/L_C}, \tag{29}$$

where Δt and $\Delta \xi$ are lags in time and space, respectively.

     To solve Eqs. (27) and (28), we put these equations in the form of the simultaneous stochastic differential equations, Eq. (25), and consider the associated covariance equations, Eq. (26). We assume that the phase-speed variance P_{cc} is stationary, yielding:

355

$$P_{cc} = \frac{Q_{cc}}{2} = \sigma_C^2. \tag{30}$$

This determines Q_{cc} from σ_C^2, which can be estimated more easily than the phase variance of nonharmonic internal tides from observations or numerical hydrodynamic modelling. Then, $P_{c\theta}$ and $P_{\theta\theta}$ evolve following

$$\frac{dP_{c\theta}}{dt} = -\frac{\overline{c}}{L_C} P_{c\theta} + \frac{\omega}{\overline{c}} \sigma_C^2, \tag{31a}$$

$$\frac{dP_{\theta\theta}}{dt} = 2\frac{\omega}{\overline{c}} P_{c\theta}. \tag{31b}$$

360   If $\overline{c}$ and L_C are constants, the solution under the initial condition $P_{c\theta} = P_{\theta\theta} = 0$ at $t = 0$ is

$$P_{\theta\theta} = 2\frac{\sigma_C^2}{\overline{c}^2} \left(\frac{\omega L_C}{\overline{c}}\right)^2 \left(\frac{\overline{c}t}{L_C} - 1 + e^{-\overline{c}t/L_C}\right). \tag{32}$$

This agrees with Eq. (12) in Zaron and Egbert (2014) if the correlation function of c' is assumed to be Eq. (29). Therefore, the above model can be seen as an extension from Zaron and Egbert (2014) to include the along-path variability of $\overline{c}$ and L_C,

which are important to deal with large water-depth change, for example, for wave propagation between a continental shelf and
deep ocean. Note that it is essential to consider the phase-speed correlation length L_C, because small correlation length makes
phase-speed variability less efficient in inducing phase variance.

The phase variance $P_{\theta\theta}$ from Eq. (31) is used as the phase variance σ_j^2 in the statistical model. Note that Eq. (31) yields
$P_{\theta\theta}$ that increases from the source towards the observation location, but we associate the final $P_{\theta\theta}$ with the source (the initial
location of integration) in the statistical model. This is because we consider internal tides observed at a location in an "inverse"
sense, and waves from remote sources are more random.

Note that the above approach considers only phase variability from travel-time variability along the deterministic (or mean)
propagation path, and neglects the effects of path variability, horizontal scattering and diffraction, and "scattering" among
vertical modes caused by density variability (through $\hat{L}_{nm}^x$ and $\hat{L}_{nm}^y$ in Eq. (A3) in Appendix A). Despite these potential
deficiencies, the approach appears to be a reasonable first approximation. For example, Buijsman et al. (2017) compared the
phase deviation calculated from the travel-time variability with those derived from a plane-wave fit to their model outputs, and
concluded that the method yielded reasonable phase spread.

It is worth noting an important detail in the above theory. Note that σ_C^2 is not only the variance of c' but also a half of the
variance of formal white noise db/dt in Eq. (28). This means that, to estimate σ_C^2 from the time series of c', for example, all
frequency components of the non-tidal variability need to be included even when low-frequency response is the interest. This
is because, as seen in the well-known example of random walk or Brownian motion, all frequency components of white noise
contribute to the low-frequency response when the noise is integrated. So, applying a subinertial and/or subtidal low-pass filter
could lead to an underestimate of σ_C^2, and hence the phase variance $P_{\theta\theta}$.

3.5 Stochastic cross-path phase difference model

We now consider the calculation of the horizontal correlation coefficients R_{ij} in Eq. (7). This requires the difference of random
phases at two locations $\Delta\Theta''$. Note that full evaluation of R_{ij} is difficult for relatively large problems because R_{ij} depend on
pairs of two source locations, which vary over the area considered (e.g., model domain), as well as possible wave propagation
paths between each source location and a fixed observation location. For this reason, a number of approximations are introduced
in the theory in this section and in numerical methods later in Section 4.4. To simplify the calculation of phase difference $\Delta\Theta''$,
we consider $\Delta\Theta''$ only in the cross-path direction in this section.

To evaluate $\Delta\theta''$ (stochastic version of the random variable $\Delta\Theta''$), we consider two waves that arrive at an observation
location from two source locations after travelling through regions of random phase-speed variability (Fig. 3b). Then, we apply
Eq. (25) to $\boldsymbol{x} = [c_i'\ c_j'\ \Delta\theta'']^T$, where c_i' and c_j' are phase speeds on paths that pass source locations $\overrightarrow{x}_i$ and $\overrightarrow{x}_j$, respectively.
The stochastic differential equations for c_i' and c_j' are obtained by applying Eq. (28) individually, except for the cross-path
correlation of random forcing. The equation for $\Delta\theta''$ is obtained by applying Eq. (27) to θ_i'' and θ_j'' individually and then taking
the difference. We take into account the variability of the mean phase speed $\bar{c}$ and the phase-speed correlation length L_C along
the propagation paths, but neglect their cross-path variability, effectively assuming that the two paths remain close to each
other. This appears to be a reasonable first approximation, except for paths that are roughly parallel to steep slopes, such as

continental shelves. Then, $\mathbf{A}$ in Eq. (25) is given by

$$
\mathbf{A} = \begin{bmatrix} -\overline{c}L_C^{-1} & 0 & 0 \\ 0 & -\overline{c}L_C^{-1} & 0 \\ \omega\overline{c}^{-1} & -\omega\overline{c}^{-1} & 0 \end{bmatrix}.
\tag{33}
$$

400 Since the distance between the two propagation paths $\Delta\eta$ (see Fig. 3b) and the correlation length can vary along the paths, the cross-path correlation of random forcing needs to be included in $\mathbf{B}$ instead of $\mathbf{Q}$, which is assumed to be time-independent. In what follows, we assume the following $\mathbf{B}$ and $\mathbf{Q}$:

$$
\mathbf{B} = \sqrt{\frac{\overline{c}}{L_C}} \frac{1}{\sqrt{1 + e^{-2|\Delta\eta|/l}}} \begin{bmatrix} 1 & e^{-|\Delta\eta|/l} & 0 \\ e^{-|\Delta\eta|/l} & 1 & 0 \\ 0 & 0 & 0 \end{bmatrix},
\tag{34a}
$$

$$
\mathbf{Q} = 2\sigma_C^2 \begin{bmatrix} 1 & 0 & 0 \\ 0 & 1 & 0 \\ 0 & 0 & 0 \end{bmatrix},
\tag{34b}
$$

405 where l is a cross-path correlation length, determined shortly. Then, the covariance equations of c_i' and c_j' have the following stationary solutions

$$
P_{c_i c_i} = P_{c_j c_j} = \sigma_C^2,
\tag{35a}
$$

$$
P_{c_i c_j} = \sigma_C^2 F(|\Delta\eta|/l),
\tag{35b}
$$

where

410
$$
F\left(\frac{|\Delta\eta|}{l}\right) = \frac{2e^{-|\Delta\eta|/l}}{1 + e^{-2|\Delta\eta|/l}}.
\tag{36}
$$

It is undesirable to have an anisotropic correlation function for phase speed; however, it appears unfortunately difficult to have cross-path correlation of the exponential form, Eq. (29), when $|\Delta\eta|$ and l vary along the paths. To keep the correlation as isotropic as possible, we set the integral scales in the along- and cross-path directions the same, yielding

$$
l = 2\pi^{-1} L_C.
\tag{37}
$$

415 Then, the evolutionary equations of $P_{c_i\Delta\theta}$, $P_{c_j\Delta\theta}$, and $P_{\Delta\theta\Delta\theta}$ are

$$
\frac{dP_{c_i\Delta\theta}}{dt} = -\frac{\overline{c}}{L_C} P_{c_i\Delta\theta} + \frac{\omega}{\overline{c}} \sigma_C^2 \left(1 - F\left(\frac{|\Delta\eta|}{l}\right)\right),
\tag{38a}
$$

$$
\frac{dP_{c_j\Delta\theta}}{dt} = -\frac{\overline{c}}{L_C} P_{c_j\Delta\theta} - \frac{\omega}{\overline{c}} \sigma_C^2 \left(1 - F\left(\frac{|\Delta\eta|}{l}\right)\right),
\tag{38b}
$$

$$
\frac{dP_{\Delta\theta\Delta\theta}}{dt} = 2\frac{\omega}{\overline{c}} \left(P_{c_i\Delta\theta} - P_{c_j\Delta\theta}\right).
\tag{38c}
$$
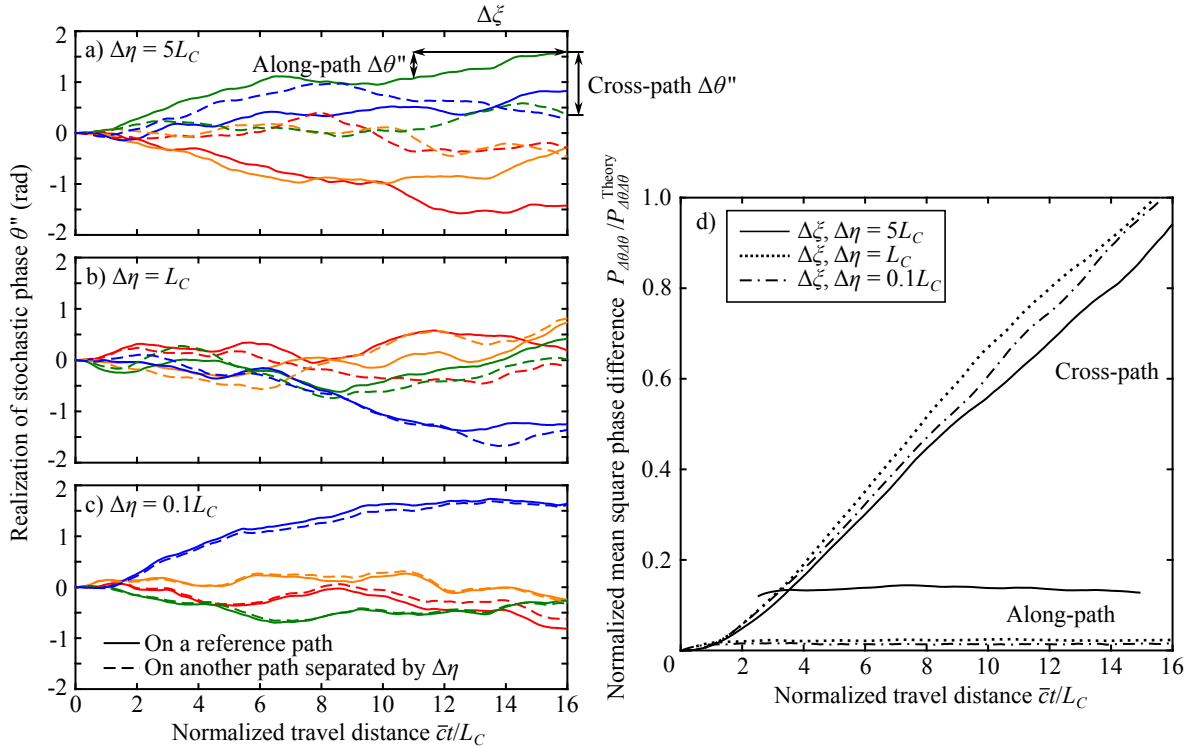
Figure 4. Example realizations of stochastic phase θ'' and variance of phase difference $P_{\Delta\theta\Delta\theta}$, calculated by numerically solving Eqs. (25), (33), and (34) with constant $\bar{c}$ and L_C. Realizations for (a) $\Delta\eta = 5L_C$, (b) $\Delta\eta = L_C$, and (c) $\Delta\eta = 0.1L_C$, and (d) normalized variance of along-path and cross-path phase difference for $\Delta\xi = \Delta\eta$, calculated from 1000 realizations. In (d), variance is normalized by theoretical value Eq. (39) for given $\Delta\eta$ at $\bar{c}t/L_C = 16$. Parameters used are $\bar{c} = 2 \text{ m s}^{-1}$, $L_C = 4.1 \times 10^4$ m, $\sigma_C^2 = 1.2 \times 10^{-2}$ m^2 s^{-2}, and semidiurnal frequency.

Generally, $P_{\Delta\theta\Delta\theta}$ needs to be calculated numerically. However, if $\bar{c}$, L_C, and $|\Delta\eta|/l$ are time-independent, the comparison of the above equations with Eq. (31) leads to the explicit solution

$$P_{\Delta\theta\Delta\theta} = 2P_{\theta\theta}\left(1 - F(|\Delta\eta|/l)\right). \tag{39}$$

This shows that the cross-path correlation length of $\Delta\theta''$ depends on the phase-speed correlation length L_C through Eq. (37). This is important because L_C can be estimated from observations or hydrodynamic modelling more easily than the correlation length of phase difference $\Delta\theta''$.

The variance $P_{\Delta\theta\Delta\theta}$ from Eq. (38) corresponds to E$\left(\Delta\Theta''^2\right)$ in Eq. (7). (As in the case of $P_{\theta\theta}$ with Eq. (31), the resultant $P_{\Delta\theta\Delta\theta}$ is associated with the sources in the statistical model.) However, note that the analysis has been simplified substantially by the assumptions introduced above. In the statistical model in Section 3.1, R_{ij} and $\Delta\Theta''$ are functions of two horizontal locations $\overrightarrow{x}_i$ and $\overrightarrow{x}_j$, but $P_{\Delta\theta\Delta\theta}$ calculated using Eq. (38) depends on along-path travel distance $\xi(t)$ and cross-path distance $|\Delta\eta|$. In particular, note that $P_{\Delta\theta\Delta\theta} = 0$ at $\Delta\eta = 0$, which implies $R_{ij} = 1$ in Eq. (7), because Eq. (38) neglects along-path

430 correlation. This choice was made because along-path correlation has the following awkward features for deterministic prop-
agation paths. Along the same propagation path, the phase variance grows following Eq. (31), so $\mathrm{E}\left(\Delta\Theta''^2\right)$ depends on the
relative distance $|\xi_i - \xi_j|$ and the phase variance reaches an upper limit (for example, in Fig. 4a–c, consider phase difference be-
tween two points separated by $\Delta\xi$ on the same solid line). On the other hand, for two paths that are widely separated compared
to the correlation length of oceanic variability (e.g., eddy A rather than eddy B in Fig. 3b), $\mathrm{E}\left(\Delta\Theta''^2\right)$ is the variance of the

435 difference of two independent random variables, and $\mathrm{E}\left(\Delta\Theta''^2\right)$ is roughly twice $P_{\theta\theta}$ in Eq. (31). It keeps growing because $P_{\theta\theta}$
depends on the whole propagation distance ξ_i and ξ_j (for example, in Fig. 4a–c, consider phase difference between solid and
dashed lines with the same colour at the same travel distance). So, $\mathrm{E}\left(\Delta\Theta''^2\right)$ tends to be much larger in the cross-path direction
than along-path direction, except near the sources (Fig. 4d). This implies larger correlation length in the along-path direction;
however, the model appears to have a deficiency in exaggerating this because it neglects path variability. Since path variability

440 is expected to grow with travel distance, averaging over modulated paths would gradually reduce the along-path correlation. To
take into account the effects of along-path correlation neglected in the theory, an empirical adjustment is introduced to $P_{\Delta\theta\Delta\theta}$
later in Section 4.4.

4 Methods

4.1 Application to VM1 semidiurnal internal tides at PIL200 location

445 To illustrate application of the proposed model suite, we took vertical mode one (VM1) semidiurnal internal tides at the
PIL200 mooring site (115.915°E, 19.435°S, ≈200 m deep) of the Australian Integrated Marine Observing System (IMOS) on
the Australian North West Shelf (Figs. 2 and 3) as an example. Part I analysed the nonharmonic VM1 to vertical mode four
(VM4) diurnal, semidiurnal, and quarterdiurnal internal tides in the observations.

In the modelling, we included the four major semidiurnal tidal constituents (M_2, S_2, K_2, and N_2) and four lowest baroclinic

450 modes (VM1–VM4). The major constituents were included as forcing of nonharmonic internal tides in the semidiurnal fre-
quency band, because it was impractical to separate nonharmonic internal tides into constituents in the PIL200 observations.
It may sound confusing to include multiple baroclinic modes to model VM1 internal tides at the PIL200 location. This is re-
quired because barotropic forcing excites not only VM1 but also higher modes, which can be converted to VM1 by topographic
interaction before arriving at the PIL200 location (see Eq. (A3) in Appendix A). To distinguish overall barotropic forcing to

455 VM1 internal tides at the PIL200 location from barotropic forcing to individual baroclinic modes in the intermediate process,
the latter is hereafter referred to as, for example, "barotropic-to-VM2" or "VM0-to-VM2" forcing.

4.2 Adjoint sensitivity and source function modelling

For adjoint frequency response analysis, we used a numerical hydrodynamic model based on the vertical-mode decomposition
of the conservation equations of volume and momentum, explained in Appendix A. We considered linear hydrostatic internal

460 tides under climatological stratification without background currents in this feasibility study. Mesoscale oceanic variability is

intentionally omitted because its effects are represented by random phase modulation in the statistical model. Since the model is linear, the adjoint model was obtained simply by transposing the matrix operator of the forward model. A sinusoidal periodic motion was assumed in the governing equations as in Eq. (21), so that the model directly calculates the adjoint frequency response function. The objective function J was VM1-induced isopycnal-displacement amplitude at the PIL200 location, which was scaled to have the value of extreme (maximum or minimum) displacement within the water column. This implicitly assumed omni-direcitonality of VM1 semidiurnal internal tides at the observation location in the adjoint model (Shimizu, 2024a), which is one of the uncertain assumptions in the model (see Discussion). We chose the above objective function partly because of simplicity and the observational uncertainty, and partly because (either surface or isopycnal) displacement amplitude has been commonly used in previous studies of nonharmonic internal tides.

Details of the model set-up were as follows. The model grid encompassed most of the Australian North West Shelf and part of the Lesser Sunda Islands in Indonesia (Fig. 2a). The horizontal coordinates were oriented in the cross-shelf (NNW–SSE) and along-shelf (SSW–NNE) directions at the PIL200 location. The horizontal grid size was $0.01°$. The model extent and grid resolution were not ideal, but limited by available computational resources. The four lowest baroclinic modes (VM1–VM4) were included in the calculation. Vertical modes were calculated using the 2019 version of GEBCO bathymetry (GEBCO Compilation Group, 2019), and stratification from the 2018 version of World Ocean Atlas (WOA) annual climatology over the 2005-2017 period (Locarnini et al., 2018; Zweng et al., 2018). TEOS-10 (McDougall and Barker, 2011) was used to calculate density. The model included horizontally-varying linear bottom friction, which was calculated using the quadratic bottom drag coefficient of 10^{-3} and the barotropic tidal current speed from the TPXO9-atlas version 5 (updated from Egbert and Erofeeva (2002)). To account for the contribution of internal tides to bottom friction in an approximate manner, the vertically-integrated kinetic energy of barotropic tides and VM1 internal tides were assumed to be the same (Wunsch, 1997). Then, horizontally varying vertical modes were used to relate the kinetic energy to near-bottom velocity induced by VM1 internal tides. The total root-mean-square near-bottom current speeds at individual grid points were calculated by taking time and phase mean, assuming random phase between the barotropic tides and VM1 internal tides. The resultant current speeds were multiplied by the quadratic drag coefficient to calculate linear friction coefficients. Other dissipative processes, such as horizontal and vertical diffusion, were neglected. Since the grid resolution was not sufficiently high to resolve internal tides in regions with shallow water depths or weak stratification, we excluded regions where celerity of each (n^{th}) vertical mode c_n was less than $0.1\,\mathrm{m\,s^{-1}}$, which roughly corresponds to four grid points per wavelength for semidiurnal tides. (In this study, the term "celerity" is deliberately used for the propagation speed of non-rotating, long, linear gravity waves with one of the vertical-mode structures.) The Flather open boundary condition (Flather, 1976; Blayo and Debreu, 2005) was applied to individual vertical modes at the open boundaries. The objective function J was defined at one grid point closest to the PIL200 location. Such a sharp "initial" condition could be problematic in numerical models in general, but it worked well in this case. The adjoint frequency response function was calculated separately for the M_2, S_2, K_2, and N_2 tidal frequencies.

The source function was calculated from the adjoint frequency response function for the four lowest baroclinic modes and barotropic currents from the TPXO9-atlas for the four major semidiurnal constituents. This provided 16 source functions in total.

4.3 Ray tracing and phase spread modelling

The phase variance $P_{\theta\theta}$ was calculated based on Eq. (31), but it required finding wave propagation paths from the PIL200 location. In this feasibility study, we took the simplest approach and calculated the propagation paths by standard ray theory (e.g., Lighthill, 1978, chap. 4.5), but applying it backwards in time starting from the observation location. The initial location was the PIL200 location and the initial angles were in $0.1°$ and $1°$ intervals for rays propagating towards offshore and onshore, respectively. Additional rays were used to ensure that some rays propagate into the southern part of the major straits in the Lesser Sunda Islands, such as the Lombok Strait. Fig. 3a shows about 1/30 of the calculated ray paths as examples. This ray tracing method had potential deficiencies, such as the neglect of interaction of vertical modes, wavelengths that are not much shorter than the continental slopes, the existence of multiple paths to some regions, and the difficulty in calculating paths passing through straits. However, these potential deficiencies were considered to be relatively minor to the overall results of this study. The reason is that travel time and the phase variance from Eq. (31) have relatively weak dependence on the details of ray paths, because they are integrated quantities of spatially variable time-mean variables, such as phase speed and its correlation length. Ray paths were calculated separately for the four lowest baroclinic modes using the M_2 frequency.

Once ray paths were calculated, Eq. (31) could be integrated along individual ray paths to calculate $P_{\theta\theta}$. However, this straightforward approach was computationally inefficient, because it needed (forward) integration from each source location to the observation location. To reduce computational cost, we exploited the fact that Eq. (31) is linear, the equations could be written in a matrix form as Eq. (15), and the associated adjoint model is Eq. (18) with the objective function being $P_{\theta\theta}$ at the observation location. The adjoint sensitivity of $P_{\theta\theta}$ at the observation location to $\boldsymbol{x} = [P_{c\theta}\ P_{\theta\theta}]^T$ at other locations were calculated by integrating the equations adjoint to Eq. (31) along individual ray paths once, backwards in time from the PIL200 location and the initial condition $\boldsymbol{w} = [0\ 1]^T$. Then, $P_{\theta\theta}$ at the observation location was calculated as the convolution of the adjoint sensitivity and the forcing along the path using Eq. (17d).

The standard ray equations and the equations adjoint to Eq. (31) were integrated backwards in time, using the 4th-order Runge-Kutta method for VM1 to VM4 semidiurnal internal tides. The time steps were 300, 450, 600, and 900 s for VM1, VM2, VM3, and VM4, respectively. The convolution Eq. (17d) for the phase variance $P_{\theta\theta}$ was calculated from the adjoint sensitivity at the full time steps of the Runge-Kutta integration. In the calculation, along-path variability of water depth, phase speed, and the Coriolis parameter were taken into account, but the frequency differences among semidiurnal constituents were neglected. The M_2 frequency was used in the modelling.

The phase-speed variance σ_C^2 in the model was chosen based on the PIL200 observations, which yielded $\sigma_{C,\mathrm{PIL200}}^2 \approx 12$, 9.5, 8.2, and 8.2×10^{-3} $\mathrm{m^2\,s^{-2}}$ for VM1, VM2, VM3, and VM4 semidiurnal internal tides, respectively (see Appendix A in Part I for the details). These values included the variability of the celerities of vertical modes (excluding seasonal cycle) and non-tidal background currents and isopycnal displacements over all frequencies. Although the observations were made on the continental shelf at ≈ 200 m water depth, the phase-speed variance of VM1 was not unreasonable for deep ocean. For example, previous numerical modelling (Zaron and Egbert, 2014; Buijsman et al., 2017) suggests $\sigma_C/\bar{c} = 1$–3% in deep ocean for VM1 semidiurnal internal tides. Since these values include only low-frequency components, they are likely to be underestimates for

530   σ_C^2, which needs to include all frequency components as explained in Section 3.4. For example, the application of a subinertial and subtidal low-pass filter reduces $\sigma_{C,\text{PIL200}}^2$ for VM1 by more than 40%. So, $\sigma_C^2 \approx 1.2 \times 10^{-2}$ m^2, which yields $\sigma_C/\bar{c} \approx 3.6\%$ assuming $\bar{c}=3$ m s^{-1}, appears to be roughly the upper limit of the current estimate of σ_C^2 for deep ocean. For higher modes, phase-speed variance appeared to be unavailable except those from Part I. These facts suggested that horizontally constant phase-speed variance was not a bad assumption, and σ_C^2 was calculated by scaling $\sigma_{c,\text{PIL200}}^2$ as

535
$$\sigma_C^2 = \alpha_C \sigma_{C,\text{PIL200}}^2, \tag{40}$$

where α_C is a model parameter. This choice was also a simple and convenient way to show the dependence of the results on σ_C^2. We used α_C varying between 0.4 and 1.0. As already explained, $\alpha_C = 1.0$ is the estimate for the PIL200 location and appears to be roughly the current upper limit for deep ocean. The choice $\alpha_C = 0.4$ ($\sigma_C/\bar{c} \approx 2.3\%$) is about the middle range of the current estimate for deep ocean, but it would be a substantial underestimate for shallow water. We arbitrarily chose

540    $\alpha_C = 0.7$ as a reference value.

     The correlation length of phase speed L_C was assumed to be proportional to the Rossby radius of deformation $R_d = \bar{c}_1/f$:

$$L_C = \alpha_L R_d, \tag{41}$$

where f is the Coriolis parameter, and α_L is a model parameter. This choice was made for two reasons. First, R_d is a common length scale used for mesoscale oceanic variability. Second, L_C is expected to vary substantially between continental shelves

545   and deep ocean, and the mean VM1 celerity $\bar{c}_1$ in the expression of R_d conveniently reflects at least some part of this variability. Note that $\bar{c}_1$ was used to calculate R_d for all the higher modes, considering that the phase-speed modulation of all vertical modes are caused by the same oceanic variability. The phase-speed correlation length appears to be rarely evaluated, but Zaron and Egbert (2014) showed that the correlation length was about three times R_d around Hawaii. This value might be affected by the smoothing scale of the reanalysis product used in their study, and is larger than the typical radius of mesoscale eddies

550   for the latitude (e.g., Klocker and Abernathey, 2014). However, phase-speed correlation could be affected by processes that have length scale larger than eddies. Since typical eddy radius is roughly R_d for the latitude range of the model domain (e.g., Klocker and Abernathey, 2014), the realistic parameter range is $\alpha_L \gtrsim 1$. We arbitrarily chose $\alpha_L = 2$ as a reference value. We also considered $\alpha_L < 1$ to understand the dependence of nonharmonic internal-tide variance on phase-speed correlation length. Note that the wavelength of VM1 semidiurnal internal tides is about 1–2 times R_d in the modelled region.

555   After the ray-based calculation, the travel time and phase variance $P_{\theta\theta}$ along the ray paths were horizontally interpolated to obtain gridded results using a Gaussian kernel. This interpolated $P_{\theta\theta}$ was used as σ_j^2 in the statistical model.

4.4   Horizontal phase correlation modelling

The horizontal correlation coefficient matrix $\mathbf{R}$ was implemented as a diffusion operator following Weaver and Courtier (2001), which is a numerical technique commonly used in data assimilation (see e.g., Bennett, 2002, chap. 3.1.6). This is because,

560   although $\mathbf{R}$ could be calculated in principle using Eqs. (7) and (38), it was prohibitive to store the whole $\mathbf{R}$ on computer memory in practice. In addition to computational benefits, the method also has an advantage that it can handle realistic boundary

shapes, which is important in oceanic applications. The method requires correlation lengths at individual grid points, which are equivalent to the standard deviation of the Gaussian function (i.e., impulse response solution to the diffusion equation). For this reason, it was convenient to approximate the first peak (around zero lag) of the horizontal correlation function as Gaussian.

565 Since Eq. (38) calculates the variance of the cross-path phase difference, Eqs. (7) and (38) yield only the cross-path correlation length σ_η, and the along-path correlation length σ_ξ is still missing. In this study, an empirical relationship between σ_η and σ_ξ was introduced, and equivalent isotropic diffusion was assumed for simplicity. Then, the method required equivalent isotropic correlation length at each grid point σ_r.

To determine σ_r, we assumed

$$570 \qquad |\Delta\eta| = \alpha_r^{-1}\Delta r \qquad\qquad (42)$$

in Eq. (38), where Δr is the distance between the sources, and α_r is an empirical parameter whose meaning is explained shortly. This assumption had an advantage that $P_{\Delta\theta\Delta\theta}$ could be integrated (backwards in time) for various values of Δr together with the ray tracing and integration of $P_{\theta\theta}$, and the results could be gridded in the same way. Substituting the resultant $P_{\Delta\theta\Delta\theta}$ into $\mathrm{E}\left(\Delta\Theta''^2\right)$ in Eq. (7) yielded the horizontal correlation function at each grid point $R(\Delta r)$, by effectively considering R_{ij}

575 between one ray path and other paths with various distance. (In Eq. (7), $\mu_i = \mu_j$ and $\varsigma_i = \varsigma_j$ were assumed.) The assumption also circumvented the dependence on ray theory to calculate $\Delta\eta$. Then, by approximating the first peak of $R(\Delta r)$ as a radial Gaussian function, we get

$$R(\Delta r) \sim \exp\left(-\frac{\Delta r^2}{2\alpha_r^2\sigma_\eta^2}\right). \qquad\qquad (43)$$

The empirical factor α_r represents two effects: anisotropy of the horizontal correlation of phase modulation, and the along-path

580 variation of cross-path distance. Typical values of α_r for these effects are considered in the following.

To estimate α_r for anisotropic phase correlation, we tentatively regard R_{ij} in Eq. (7) as correlation function $R(\Delta\xi, \Delta\eta)$ ($\Delta\xi$ is the along-path distance of the two sources), and compare its integral scale with that of the equivalent isotropic correlation function $R(\Delta r)$. Assuming that the correlation functions are Gaussian and equating the integrals, we get

$$\int_{-\infty}^{\infty}\int_{-\infty}^{\infty}\exp\left(-\frac{\Delta\xi^2}{2\sigma_\xi^2}-\frac{\Delta\eta^2}{2\sigma_\eta^2}\right)d\Delta\xi d\Delta\eta \approx 2\pi\int_0^{\infty}\Delta r\exp\left(-\frac{\Delta r^2}{2\sigma_r^2}\right)d\Delta r, \qquad\qquad (44)$$

585 where σ_ξ is unknown standard deviation in the along-path direction. This yields the relationship of the integral scales

$$\sigma_\xi\sigma_\eta \approx \sigma_r^2. \qquad\qquad (45)$$

The comparison of Eqs. (43)–(45) shows that $\alpha_r = \sqrt{\sigma_\xi/\sigma_\eta}$, and $\alpha_r = 1$ for isotropic correlation function ($\sigma_\xi = \sigma_\eta$). Note the relatively weak dependence of α_r on σ_ξ. For example, the correlation function is highly anisotropic (approximately one dimensional in the cross-path direction) for $\sigma_\xi = 9\sigma_\eta$, but it yields $\alpha_r = 3$.

590 To estimate α_r for the along-path variation of cross-path distance, we consider the linear variation of cross-path distance $|\Delta\eta|$ between the observation location and source locations. Since the distance between the sources is Δr, an intuitive value

for average $|\Delta\eta|$ over the paths is $\alpha_r = 2$ (i.e., the mean is a half of the maximum at one end). A more accurate way to evaluate α_r is to consider the path average of the Gaussian correlation function calculated tentatively with $\alpha_r = 1$, and then determine the equivalent α_r for the same Δr. This shows that $\alpha_r = 2$ is a reasonable choice. However, note that ray tracing suggests large along-path variability of $|\Delta\eta|$ (Fig. 3a). For example, cross-path distance during the propagation can be larger than the distance between the two source locations.

Based on the above consideration, σ_r was calculated from Eqs. (7), (38), and (42) as follows. Considering both anisotropy of the phase correlation and the along-path variation of cross-path distance, α_r between 1 and 5 appeared to be reasonable. To understand the dependence of nonharmonic internal-tide variance on horizontal phase correlation, it was also beneficial to consider $\alpha_r \ll 1$, which corresponds to the lack of horizontal phase correlation. We considered α_r to be a uncertain model parameter, and varied the value to test the dependence of the results on this parameter. We arbitrarily chose $\alpha_r = 3$ as a reference value. From the equivalent isotropic correlation function obtained from Eqs. (7), (38), and (42), σ_r was calculated by the least-squares fit of the Gaussian shape to the first peak of the correlation function. (This means $\sigma_r = \alpha_r \sigma_\eta$ in Eq. (43), although σ_η was not calculated explicitly.) Since the correlation function $R(\Delta r)$ generally has a broader tail than the Gaussian distribution, the integral scale was unsuitable. The least-squares fitting was applied where $R(\Delta r) > 0.5$, with the aim of getting reasonable σ_r at $R(\Delta r) \approx 0.6$ (corresponding to one standard deviation). This fitting procedure did not always work well in shallow water where stratification was weak. To keep σ_r within a realistic range, the grid size and $\alpha_r L_C$ were imposed as the lower and upper limits of σ_r, respectively. This σ_r was used as the correlation length in the diffusion model.

In addition to σ_r, the diffusion operator method also required normalization factors that impose $R_{ii} \approx 1$ after applying the diffusion operator (i.e., the matrix $\mathbf{\Lambda}$ in Weaver and Courtier (2001)). The normalization factors were calculated by the ensemble method explained in Weaver and Courtier (2001). We used 200 ensemble members, which correspond to the standard error of 5% in the normalization of $\mathbf{R}$.

As in the ray tracing and phase spread modelling, the calculations of correlation lengths were done separately for the four lowest baroclinic modes using the M_2 frequency. The frequency differences among semidiurnal constituents were neglected.

4.5 Calculation of nonharmonic variance source function

The nonharmonic variance source function was calculated from Eq. (12), using s_{phys} from the source function, $\mathbf{\Sigma}$ calculated from the phase variance $P_{\theta\theta} = \sigma_j^2$, and $\mathbf{R}$ implemented as a diffusion operator with the equivalent isotropic correlation length of phase modulation σ_r; however, it required one more assumption, because it was not obvious which phase spread and phase correlation should be applied to each source function. For example, if higher modes are directly excited by barotropic forcing and converted to VM1 near the sources, and then the VM1 internal tides propagate to the observation location, the phase spread and correlation lengths for VM1 should be applied to the source functions for higher modes, because the phases are modulated as VM1 internal tides. However, if higher modes are directly excited by barotropic forcing, propagate as higher modes, and then converted to VM1 near the observation location, the phase spread and correlation lengths for higher modes should be applied to the source functions of respective higher modes. The latter scenario was assumed in this study, because the PIL200 location is located in the continental shelf/slope region.

4.6 Equivalent degrees of freedom

It is convenient to have an estimate of the number of independent sources, which is one of the input parameters to the statistical model and an indicator whether the central limit theorem is applicable. It should be provided by s_{stat} in Eq. (11) in principle, but unfortunately the use of $\mathbf{R}^{T/2}$ makes the estimate of statistically independent sources non-unique, as explained in Section 3.1.

630   Nonetheless, it would still be more useful to have a rough estimate than no estimate. In this study, the equivalent degrees of freedom of each grid point were calculated by dividing the horizontal cell area by the squared correlation length of phase modulation, in a similar way to calculating the degrees of freedom of a time series using the integral time scale. This choice was made because the diffusion operator method for $\mathbf{R}$ diffuses the source function as the simple example in Eq. (14), rather than concentrates it as the example in Eq. (13). Note that, for horizontally distributed sources, the absolute number of sources (or

635   degrees of freedom) is not useful because there are grid points that have small or negligible contributions to the total variance, but such points are also counted as independent sources. So, we considered the functional relationship between cumulative variance and cumulative number of independent sources (e.g., degrees of freedom to explain 90% of modelled variance) after sorting the sources in descending order of per-cell and per-mode contributions to the variance.

5 Results

5.1 Adjoint frequency response function

640

The adjoint frequency response function of VM1-induced isopycnal displacement at the PIL200 location to the barotropic-to-VM1 forcing qualitatively shows a pattern of internal waves spreading from a point source, but affected by topography-induced variation of the propagation speed (Fig. 5a). For internal-wave signals propagating offshore, wave spreading gradually reduces the magnitudes. By the time the signals reach the Indonesian archipelago, the magnitudes are reduced by a factor of more than

645   10. For internal-wave signals propagating towards the Australian coast, the wavelengths decrease rapidly because shallower water depths and weaker stratification reduce the propagation speed. The signals disappear on the shelf shallower than 100 m, partly because of bottom friction, and partly because the grid resolution gradually becomes insufficient to adequately resolve internal tides there. This numerical dissipation does not change the overall results of this study, because the shallow shelf has mild slopes and hence no important sources of internal tides at the PIL200 location.

650   The adjoint frequency response function to the barotropic-to-VM2 forcing also shows a pattern of internal waves spreading from a point source (Fig. 5b). The magnitudes are smaller than the VM1 signals because the VM2 (and other higher-mode) signals result from the topographic conversion of VM1 signals on the continental slope. The shorter wavelength shows that the signals are propagating as free VM2 internal-wave signal, at least as a first approximation. These features justify our choice of applying the phase spread and horizontal phase correlation for VM2 to the VM2 source function (Section 4.5). This may

655   sound nothing special but should not be taken for granted, because the spatial pattern would be very different if the topographic conversion occurs near the sources, or if VM2 signals result from directly forced response rather than free-wave response.
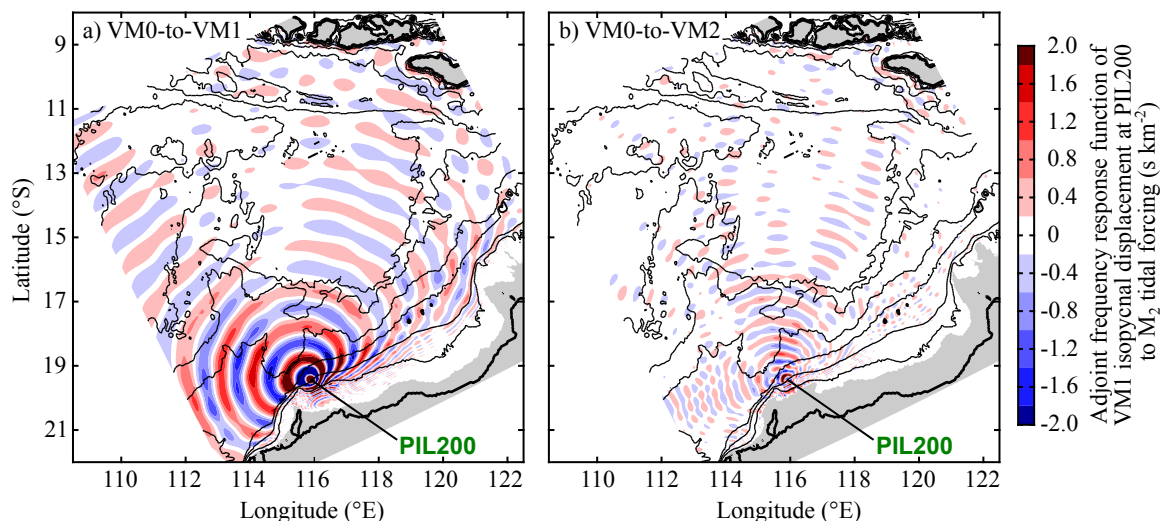
Figure 5. Adjoint frequency response function of vertical-mode-one (VM1)-induced isopycnal displacement at PIL200 location to M_2 tidal forcing at other locations (at zero Greenwich phase lag). It corresponds to $\tilde{\lambda}$ in Eq. (23). (a) Barotropic-mode (VM0) to VM1 forcing, and (b) VM0 to vertical-mode-two (VM2) forcing. Black lines show isobaths at 10, 100, 200, 500, 1500, 3000, and 5000 m water depths. Grey shading shows regions where celerity is less than $0.1\,\mathrm{m\,s^{-1}}$.

Additionally, these different scenarios affect which phase spread and horizontal phase correlation should be applied to the VM2 (and higher-mode) source function.

5.2 Source function

660 The source function was calculated simply by multiplying the forcing function (Fig. 2) and the complex conjugate of the adjoint frequency response function (Fig. 5). Fig. 6 shows the source function of VM1 M_2 internal tide at the PIL200 location as an example. It shows alternating signs at the wavelength of VM1 M_2 internal tide. Physically, it means, for example, that the internal tides generated at half a wave length away from the PIL200 location and then propagated there have the opposite phase from those locally and currently generated at the location. So, these waves tend to cancel each other, and the opposite

665 signs in the source function reflect this wave cancelling. Although the adjoint frequency response function decays with distance (Fig. 5a), remote locations with strong barotropic tides and/or steep bottom slopes can be as strong sources as those near the observation location. For example, the magnitudes of the source function in the straits of the Indonesian archipelago, which are well known source regions of internal tides, are comparable to those on the Australian shelf.

5.3 Phase spread

670 VM1 internal tides from most of the model domain except the Australian shelf are only partially random (Fig. 7b). The travel time τ for VM1 semidiurnal internal tides calculated by ray theory increases roughly radially from the PIL200 location
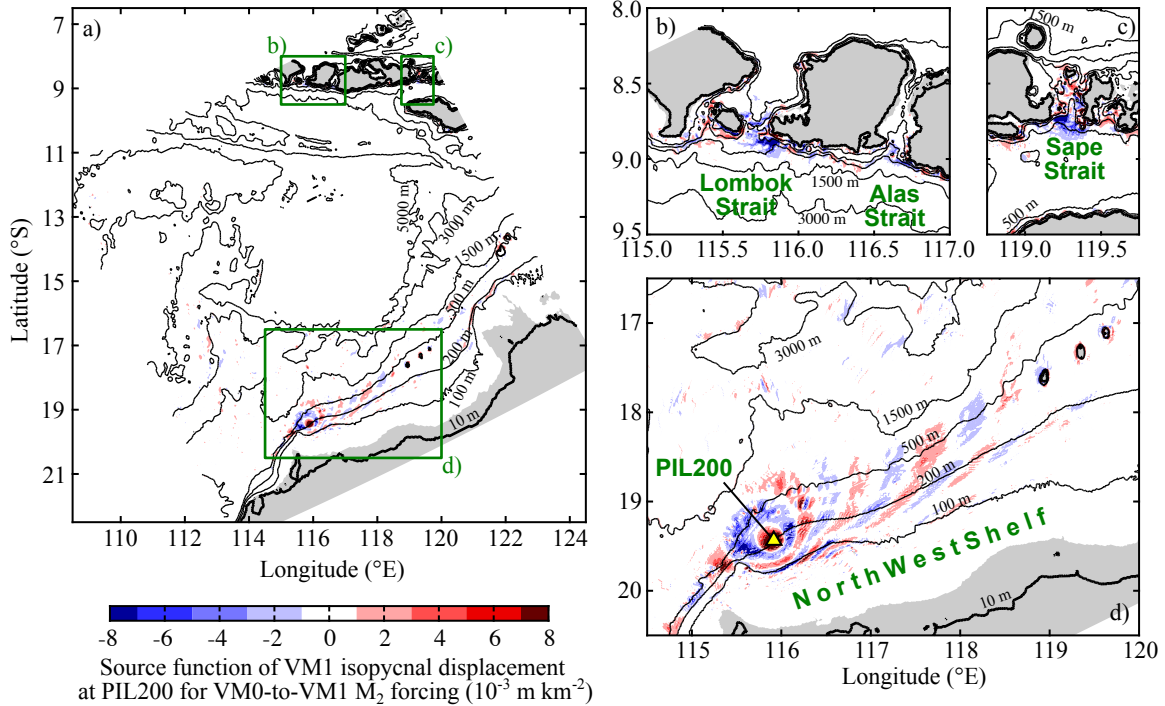
Figure 6. Source function of vertical-mode-one (VM1)-induced isopycnal displacement at PIL200 location for barotropic (VM0)-to-VM1 M_2 forcing (at zero Greenwich phase lag). It corresponds to s in Eq. (23). Panels (b-d) show zoomed views of green boxes in (a). Grey shading shows regions where VM1 celerity is less than $0.1\,\mathrm{m\,s^{-1}}$.

(Fig. 7a), which agrees with the adjoint sensitivity (Fig. 5a). A clear exception is the Australian shelf where τ grows quickly because of small group velocity. The phase variance $P_{\theta\theta} = \sigma_j^2$ also increases roughly radially, but the rate of increase is faster on the shelf because the phase-speed variance σ_C^2 relative to the squared mean phase speed $\bar{c}^2$ is much larger there (Fig. 7b).

675 Note that $\sigma_j > 1$ is a convenient threshold for mostly random sources (see Eq. (4d); also Fig. 2d in Part I for illustration).

Unlike VM1, VM2 internal tides are mostly random (Fig. 7e). This is partly because the phase-speed variance σ_C^2 relative to the squared mean phase speed $\bar{c}^2$ is larger for VM2 than VM1, so the rate of increase of phase variance is higher. Another reason is that VM2 internal tides have about twice the travel time compare to VM1, and hence VM2 has more time to be affected by random oceanic variability (Fig. 7d).

680 5.4 Horizontal correlation of phase modulation

The equivalent isotropic correlation length of phase modulation σ_r shows an order-of-magnitude variability between the deep ocean and continental shelf for VM1 (Fig. 7c), and tends to have magnitude comparable to but smaller than $\alpha_r L_C$ over a large part of the model domain. The reason for this can be seen by considering Eqs. (7) and (39) in the limit of small $P_{\theta\theta} = \sigma_j^2$, which suggests the length scale $2\pi^{-1}\alpha_r L_C$. For example, the gradual increase of σ_r towards north reflects the latitudinal variation
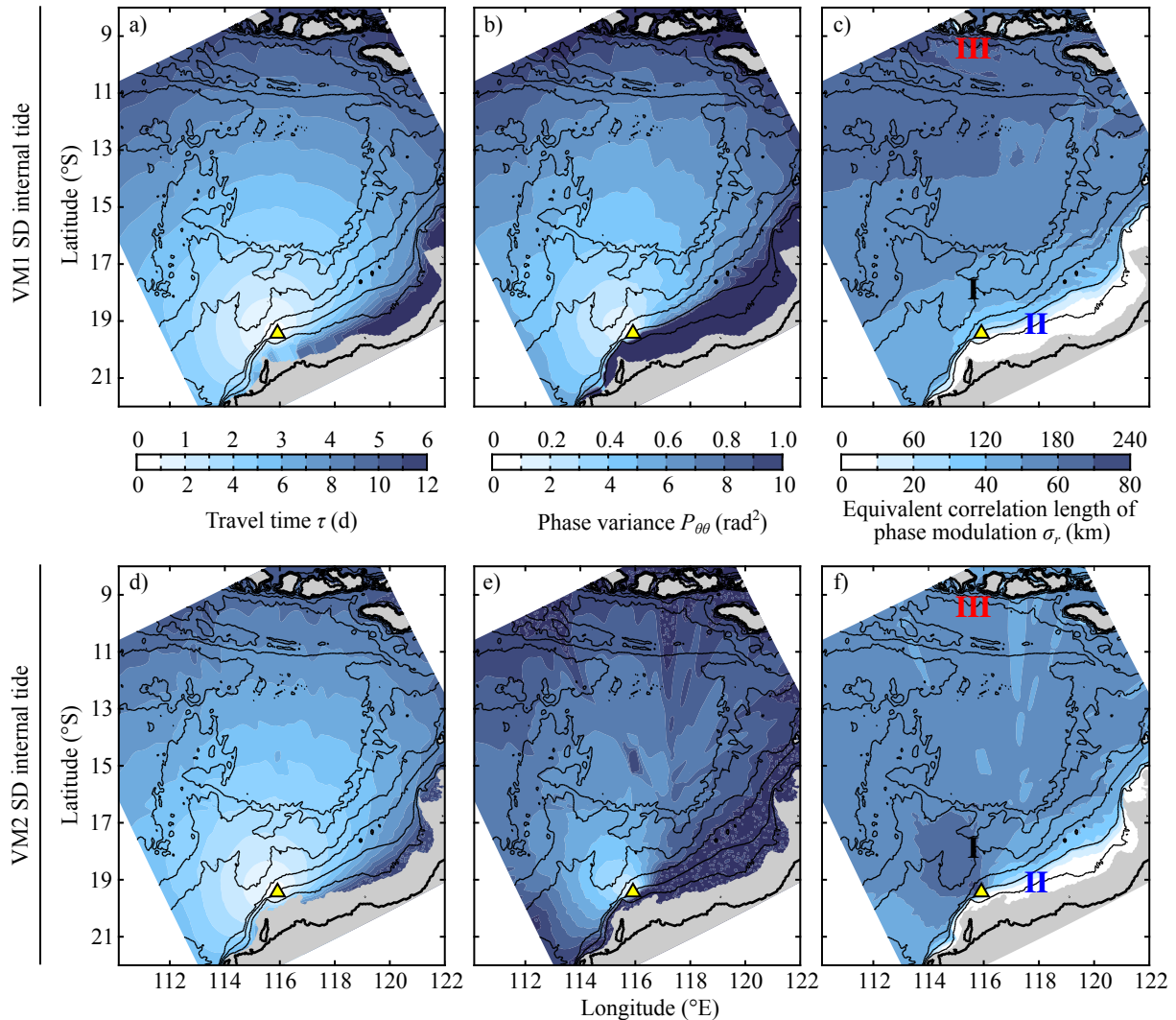
Figure 7. Maps of variables related to phase modulation of semidiurnal (SD) internal tide at PIL200 location in reference case: $(\alpha_C, \alpha_L, \alpha_r) = (0.7, 2, 3)$. Left, middle, and right panels show travel time, phase variance, and equivalent isotropic correlation length of phase modulation, respectively. Upper and lower panels are for vertical mode one (VM1) and mode two (VM2), respectively. Note the different scales for upper and lower panels. Yellow triangles indicate PIL200 location. Roman numerals in panels (c,f) show locations where correlation functions are shown in Fig. 8. Black lines show isobaths at 10, 100, 200, 500, 1500, 3000, and 5000 m water depths. Grey shading shows regions where celerity is less than $0.1 \, \mathrm{m\,s^{-1}}$.

685 of the Rossby radius of deformation, which is assumed to be proportional to L_C. The small σ_r on the continental shelf results from small celerity (and hence small Rossby radius of deformation). The modelled equivalent isotropic correlation function at three contrasting locations are shown in Fig. 8a. The correlation function generally has a broader tail than the Gaussian
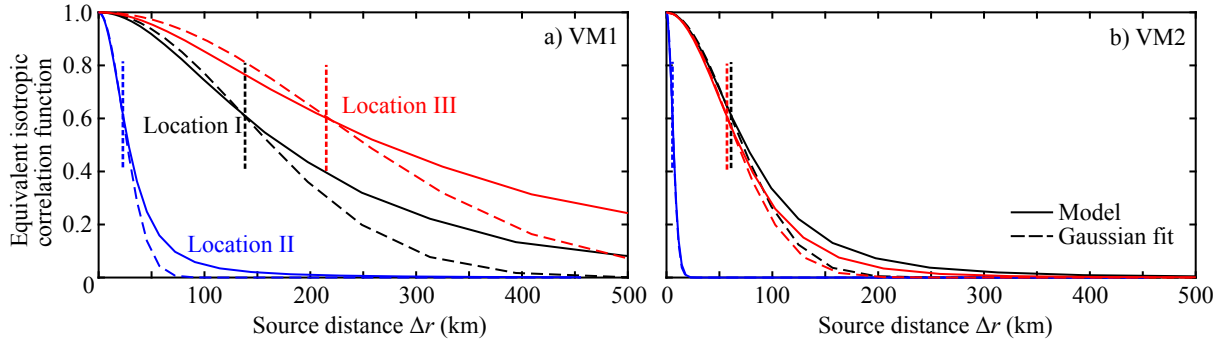
Figure 8. Examples of equivalent isotropic correlation functions of phase modulation at locations I, II, and III indicated in Fig. 7c,f. (a) Vertical mode 1 (VM1) and (b) mode 2 (VM2). Dotted vertical lines indicate correlation length σ_r determined by least-squares fit of Gaussian function.

Table 1. Nonharmonic vertical-mode-one (VM1) semidiurnal internal-tide variance (Var) in different regions and associated equivalent degrees of freedom (DoF) that explain 60% and 90% of variance in reference case: $(\alpha_C, \alpha_L, \alpha_r) = (0.7, 2, 3)$. Variance is based on extreme (maximum or minimum) isopycnal displacement within water column. Regions are shown in Fig. 9.

Region	VM1 M_2 only			VM1–4, M_2, S_2, K_2, N_2		
	Var (m^2)	DoF (60%)	DoF (90%)	Var (m^2)	DoF (60%)	DoF (90%)
LOC	3.2	12	23	6.0	65	247
NWS	4.9	18	40	8.2	92	457
LAS	7.9	1	2	13.5	10	50
SS	0.4	0	1	2.6	14	95
IND	2.9	6	16	7.5	263	1619
Total	19.4	37	82	37.8	443	2467

function. The modelled and fitted correlation functions agree around the correlation value of 0.6, which corresponds to one standard deviation of the Gaussian function.

690   The equivalent isotropic correlation length σ_r for VM2 is substantially smaller than VM1 (Fig. 7f) and does not have the rough relationship with L_C, although the same L_C is used for VM1 and VM2. This is because the phase variance $P_{\theta\theta} = \sigma_j^2$ is much larger for VM2 than VM1 (Fig. 7b,e), which makes the gradient of $P_{\Delta\theta\Delta\theta}$ around $|\Delta\eta|/l \ll 1$ larger (see Eq. (39)) and the decay of the exponential function in Eq. (7) faster. As a result, the latitudinal variation does not exist for VM2, but the order-of-magnitude variability between the deep ocean and continental shelf remains. Fig. 8b shows that the modelled and

695   fitted correlation functions agree well for correlation values larger than 0.6 for VM2.
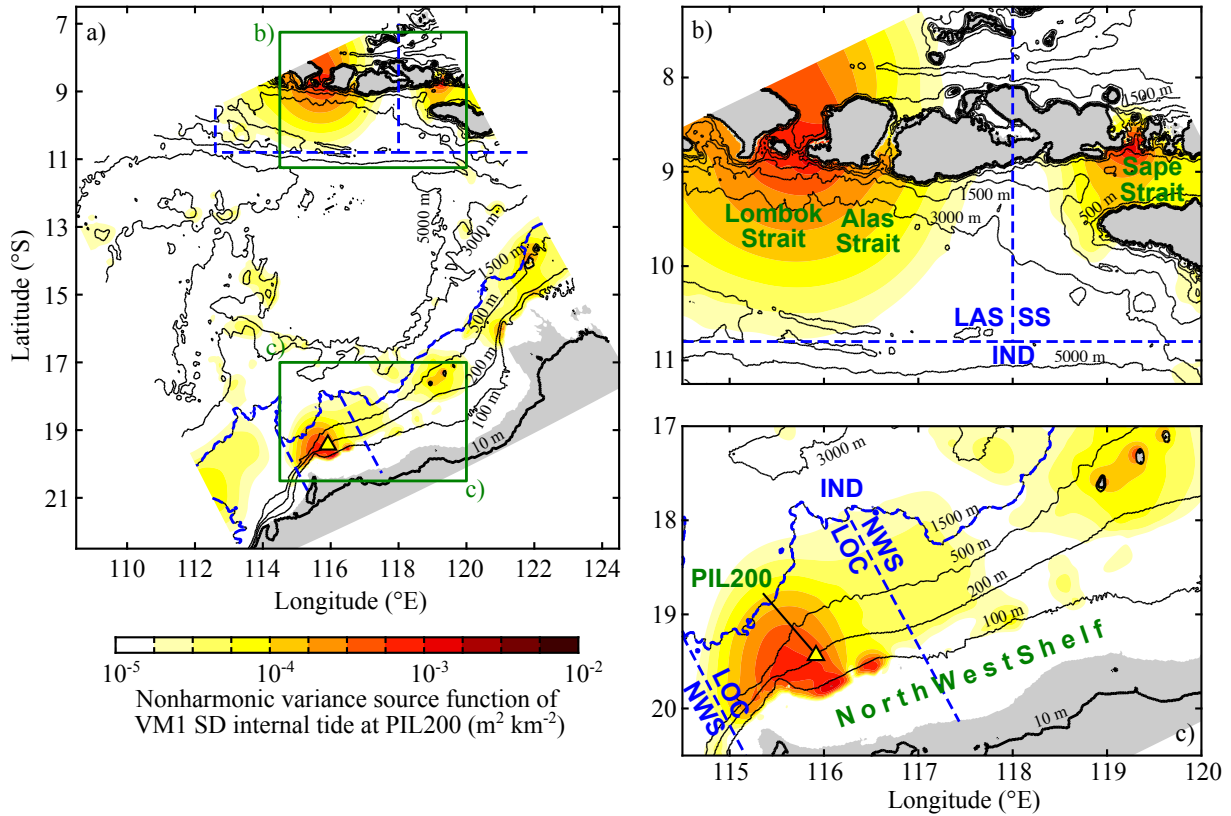
Figure 9. Nonharmonic variance source function of isopycnal displacement induced by nonharmonic vertical-mode-one (VM1) semidiurnal (SD) internal tide at PIL200 location in reference case: $(\alpha_C, \alpha_L, \alpha_r) = (0.7, 2, 3)$. Lowest four baroclinic modes and four major semidiurnal constituents are included. Panels (b,c) show zoomed views of green boxes in (a). Grey shading shows regions where VM1 celerity is less than $0.1\,\mathrm{m\,s^{-1}}$.

Table 2. Contributions of different vertical modes (VM) and tidal constituents to nonharmonic VM1 semidiurnal internal-tide variance (in $\mathrm{m^2}$) at PIL200 location in reference case: $(\alpha_C, \alpha_L, \alpha_r) = (0.7, 2, 3)$. Variance is based on extreme (maximum or minimum) isopycnal displacement within water column.

	M_2	S_2	K_2	N_2	Total
VM1	19.4	6.8	0.8	0.5	27.5
VM2	4.7	1.6	0.2	0.1	6.6
VM3	1.9	0.4	0.1	0.0	2.4
VM4	0.9	0.2	0.0	0.0	1.2
Total	26.9	9.0	1.1	0.7	37.8

5.5 Contributions of different source regions, vertical modes, and tidal constituents

The results of the modelling provide the contributions of different source regions, vertical modes, and tidal constituents to the modelled nonharmonic internal tides, and their dependence on the model parameters. We look at different contributions using the reference case $(\alpha_C, \alpha_L, \alpha_r) = (0.7, 2, 3)$ as an example in this section, and then the parameter dependence in the next

700 section. The total modelled nonharmonic VM1 semidiurnal internal-tide variance is 38 m^2 in the reference case, compared to the observed variance of 45 ± 12 m^2 (confidence interval based on twice the standard error). As explained in Section 4.2, the variance is calculated based on VM1-induced extreme (maximum or minimum) isopycnal displacements within the water column. The variance values can be converted to vertically integrated potential energies in J m^{-2} by multiplying 7.6, and the variance of surface displacements in m^2 by multiplying 7.1×10^{-7} (without seasonal variation).

705 The contributions of different regions are shown in Fig. 9 as the map of nonharmonic variance source function, and in Table 1 as regionally integrated contributions. The following regions are arbitrary chosen for illustration purposes. The LOC region is the local region near the PIL200 location on the Australian North West Shelf shallower than 1500 m, and the NWS region is the Australian shelf region excluding the LOC region. The LAS and SS regions cover the Lombok and Alas straits and Sape Strait, respectively. The IND region is the rest of the model domain, mostly deep Indian Ocean. These regions are

710 indicated by dashed blue lines in Fig. 9. Fig. 9 shows that important source regions are the Australian shelf, and the straits in the Indonesian archipelago. The nonharmonic variance source function appears much smoother than the source function in Fig. 6, because the diffusion operator that approximates the correlation coefficient matrix $\mathbf{R}$ is applied, and the correlation lengths are relatively large (Fig. 7c,f). The horizontal scale of the nonharmonic variance source function is smaller than the correlation length for VM1 (Fig. 7c). This is partly because higher modes have smaller correlation lengths (Fig. 7f), and partly because the

715 diffusion operator averages the opposing contributions from the source function (e.g., red and blue patches in Fig. 6) when the correlation length is comparable to or larger than the wavelength, which reduces the length scale of the nonharmonic variance source function. However, note that the locations of sources in the nonharmonic variance source function are uncertain within the correlation length of phase modulation in the current approach, as explained in Section 3.1. This is why contributions from relatively large regions are compared in Table 1.

720 Table 1 shows that remote regions are more important sources of the nonharmonic internal tides than local sources. For example, the contributions of the Australian shelf is smaller than those of the Indonesian straits, and the local contribution on the Australian shelf is smaller than the rest of the shelf. This is because remote sources can be as strong as local sources before phase modulation (Fig. 6), and it takes time for random phase-speed variability to make internal tides nonharmonic (Fig. 7b,e). Although the magnitude of the nonharmonic variance source function in the deep ocean (IND region) is nearly two orders of

725 magnitude smaller than the peak values in the major sources (Fig. 9), Table 1 shows that the overall contribution is substantial because it occupies much larger area than the other regions. Fig. 9 also suggests that, although we used a relatively large model domain for available computational resources, the current modelling is likely to have missed remote sources. It is likely that at least a few m^2 of variance is missing from deep Indian Ocean to the west of the model domain.
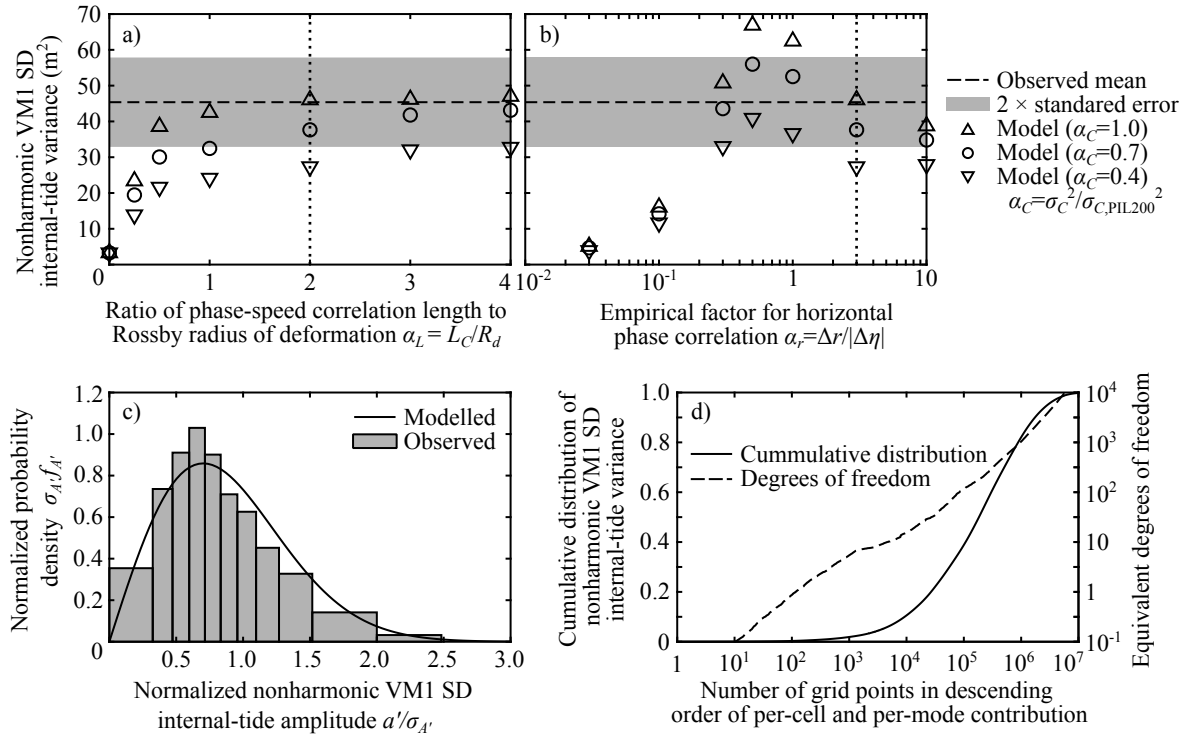
Figure 10. Parameter dependence and probability distribution of nonharmonic vertical-mode-one (VM1) semidiurnal (SD) internal tide at PIL200 location. (a) Dependence of internal-tide variance on normalized phase-speed variance α_C and ratio of phase-speed correlation length to Rossby radius of deformation α_L, (b) dependence on α_C and empirical parameter for horizontal correlation of phase modulation α_r, (c) comparison of modelled and observed probability distribution function of envelope amplitude normalized by standard deviation, and (d) cumulative distribution of per-cell and per-mode contribution to internal-tide variance and equivalent degrees of freedom as a function of grid points (sorted in descending order of per-cell and per-mode contribution). Panels (a) and (b) show results for $\alpha_r = 3$ and $\alpha_L = 2$, respectively. Reference parameters $(\alpha_C, \alpha_L, \alpha_r) = (0.7, 2, 3)$ are used in (c) and (d). In (a) and (b), dotted vertical lines indicate values used in reference case.

Table 2 shows the contributions of different vertical modes and tidal constituents to the modelled variance. The tabular entry

730 for VM2 and M_2 represents, for example, the contribution of VM2 internal tide that is excited by the M_2 barotropic forcing, and then converted to VM1 before arriving at the PIL200 location. Regarding the contributions of different vertical modes, the model results show that VM1 contributes about 3/4 of the total variance, and the contributions decrease with increasing mode number. Regarding the contributions of barortropic forcing from different tidal constituents, M_2 and S_2 forcing contribute roughly 3/4 and 1/4 of the total variance, respectively. The contributions of K_2 and N_2 are small (1.8 m^2). The VM1 directly

735 forced by M_2 alone contributes roughly a half of the total variance. So, VM1 and M_2 are dominant, but focusing only on VM1 and M_2 would cause substantial underestimation of the nonharmonic semidiurnal internal-tide variance in this case.

5.6 Dependence on model parameters and comparisons with observations

The results shown in the previous section are based on the reference model parameters, but the parameters have relatively large uncertainty. In this section, we investigate the dependence of the results on the model parameters, and compare the results with observations at the PIL200 location. The model parameters are varied beyond the realistic range for process understanding.

The results show that the modelled nonharmonic internal-tide variance strongly depends on the variance (α_C or σ_C^2) and correlation length (α_L or L_C) of phase speed (Fig. 10a). These parameters affect the nonharmonic internal-tide variance in two ways. First, they determine the partitioning of the variance into harmonic and nonharmonic components through the phase variance σ_j^2 (see Eq. (4)). Second, they affect the phase correlation length σ_r through μ_j and ς_j in Eq. (7), as well as the variance of horizontal phase difference $P_{\Delta\theta\Delta\theta}$ in Eq. (38). The dependence on α_L shows that it is essential to consider the phase-speed correlation length (see the small variance at $\alpha_L = 0$ in Fig. 10a), because phase-speed variability with small correlation length is inefficient in producing phase variance (see Eq. (32)). The dependence on α_L gradually decreases with increasing α_L for a few reasons. First, the ratio of the variance partitioned to nonharmonic component (ς_j^2 in Eq. (4)) increases with the phase variance σ_j^2, but the rate of increase becomes much slower for $\sigma_j^2 > 1$ (see Eq. (4d); also Fig. 2d in Part I for illustration). Second, the horizontal phase correlation tends to increase nonharmonic internal-tide variance as explained in Section 3.1, but the increase ceases when the equivalent isotropic correlation length σ_r becomes comparable to the internal-tide wavelength. This is because regions separated by half a wavelength tend to have opposing contributions to internal-tide amplitude (see blue and red patches in Fig. 6), and the opposing contributions are averaged in Eq. (11) when the correlation length is larger than half the wavelength.

The nonharmonic internal-tide variance also strongly depends on α_r (Fig. 10b). The dependence illustrates the aforementioned roles played by the phase correlation length σ_r and internal-tide wavelength more clearly, because σ_r is roughly proportional to α_r. The phase correlation increases the nonharmonic internal-tide variance when α_r is small. Although $\alpha_r \ll 1$ (negligible horizontal correlation) is unrealistic, small variance in this limit shows that it is essential to consider horizontal phase correlation for gridded sources, as explained in Section 3.1. When α_r becomes larger, the nonharmonic internal-tide variance decreases gradually with increasing α_r by the averaging of sources with opposite phases. The peak of the variance should occur when σ_r is around a quarter of the wavelength. Considering that the internal-tide wavelength is 1–2 times the Rossby radius of deformation in the modelled region and σ_r tends to be comparable but smaller than $\alpha_r L_C$ for VM1, this suggests $\alpha_L \alpha_r$ is roughly 1/2 at the peak. Fig. 10b shows the peak around $\alpha_r \approx 1/2$ for $\alpha_L = 2$. This shows that anisotropy of the horizontal correlation of phase modulation is an important controlling parameter for a realistic parameter range ($\alpha_L \gtrsim 1, \alpha_r \gtrsim 1$), especially if $\alpha_L \approx 1$. More generally, the result shows that the ratio of the correlation length of phase modulation and internal-tide wavelength is important for nonharmonic internal-tide variance.

The comparison of the model results and the PIL200 observations shows that the model results are not inconsistent with the observations for a realistic parameter range ($\alpha_L \gtrsim 1, \alpha_r \gtrsim 1$), although the modelled variance tends to be smaller than the observed mean. The larger phase-speed variance case ($\alpha_C = 1.0$) used phase-speed variance from the PIL200 location on the continental shelf, which provides phase-speed variance that appeared to be roughly the upper limit of previous estimates for

deep ocean. In this case, the model results are around the observed mean for $\alpha_L \geq 1$. The smaller phase-speed variance case ($\alpha_C = 0.4$) used phase-speed variance that is about the middle of previous estimates for deep ocean, but is an underestimate for shallow water. So, it is reasonable that the modelled variance is around or below the approximate 95% confidence interval for $\alpha_L \geq 1$. In the reference case for phase-speed variance ($\alpha_C = 0.7$), the model results are between the observed mean

775 and the lower bound of the approximate 95% confidence interval for $\alpha_L \geq 1$. Considering the number of assumptions and simplifications used in the model suite, the results are encouraging. This demonstrates the feasibility of the proposed modelling framework and model suite.

Finally, we compare the modelled and observed PDFs of nonharmonic VM1 semidiurnal internal tides (Fig. 10c). Since the modelled and observed variance are not the same, PDFs are normalized by the respective standard deviation. The normalized

780 PDFs compare well. This result and analyses in Part I suggest that the degrees of freedom (DoF) of the modelled nonharmonic internal tides are high enough for the central limit theorem to be applicable. The estimate of effective DoF suggests that roughly 440 and 2500 effectively independent sources are required to explain 60% and 90% of the total modelled variance (Fig. 10d, Table 1). Since higher modes have shorter phase correlation length and hence more DoF, Table 1 also shows effective DoF only for the VM1 M_2 component. The estimate suggests more than 30 independent sources are required to explain 60% of the

785 variance. Although these DoF are rough estimates, the results of Part I suggest that these DoF are high enough for the central limit theorem to be applicable in oceanic conditions. This justifies the assumptions used in the model suite, such as the use of Eq. (11).

6 Discussion

This paper developed a new framework and model suite for process-based modelling of nonharmonic internal tides by com-

790 bining adjoint, statistical, and stochastic approaches. This required the development of a new method called adjoint frequency response analysis and new stochastic models based on stochastic differential equations. (The adjoint frequency response analysis is new in physical oceanography to my knowledge, although the use of the adjoint method in many fields makes more comprehensive literature survey difficult.) The application of the model suite to nonharmonic vertical-mode-one (VM1) semidiurnal internal tides at the PIL200 location on the Australian North West Shelf added further support that the phase modulation

795 process is described by travel-time variability along deterministic (or mean) propagation paths (Zaron and Egbert, 2014) as a first approximation. The correlation length of phase speed and anisotropy of the horizontal correlation of phase modulation were found to be important parameters controlling the nonharmonic internal-tide variance, in addition to phase-speed variance which has been identified in previous studies (Zaron and Egbert, 2014; Buijsman et al., 2017). Furthermore, the nonharmonic variance source function was shown to be a new convenient tool to identify important source regions of nonharmonic internal

800 tides. These are the major novel contributions of this study.

In the proposed stochastic models, it was aimed to model stochastic wave-phase variables based on the variance and correlation length of phase speed as much as possible. This is because these parameters can be obtained more easily than the phase statistics of nonharmonic internal tides, for example, from reanalysis products that do not include tides. Hopefully, this leads

to wider application of the proposed stochastic models in the future. In this study, the phase-speed variance and correlation length were assumed to be proportional to the observed variance at the PIL200 location and the Rossby radius of deformation, respectively. These choices were made partly because this was a feasibility study, partly because it was convenient to show the parameter dependence, and partly because it was not computationally cheap to calculate the horizontal distribution of phase-speed variance and correlation length from reanalysis products, especially with capturing the variance from a wide frequency range. The use of more realistic phase-speed variance and correlation length would be beneficial for comparing modelled and observed variance in the future.

The proposed model suite was aimed to be simple enough to include essential processes only, and this study appears to have achieved the aim; however, the modelled variance tended to be smaller than the observed mean for a realistic range of the model parameters (Fig. 10a,b). Furthermore, the modelled variance might be more underestimated than it appears in Fig. 10a,b, because only semidiurnal internal tides were considered in the model suite, but the PIL200 observations showed that the nonharmonic quarterdiurnal internal tides had roughly 20% of the variance of the semidiurnal counterpart. The underestimation could have been caused simply by numerical reasons (or available computational resources), including insufficient model domain size and grid resolution. It appears likely that at least a few to half a dozen m^2 of variance were missing for numerical reasons. But the underestimation might also be caused by missing processes of secondary importance, and it would be worth mentioning three potential causes here. First, the amplitude variability of wave sources was neglected. Part I showed that the amplitude variability tends to increase nonharmonic internal-tide variance (see Shimizu, Companion Paper, Eq. (20b)), although it is less important than the phase variability. Second, the variability of propagation paths was neglected in the model. The results in Zaron and Egbert (2014), Buijsman et al. (2017), and this study suggest that it is a good first approximation, but the variability might have important second-order effects. It tends to increase phase modulation and make its horizontal correlation more isotropic (effectively larger α_L and smaller α_r), both of which increase nonharmonic internal-tide variance (Fig. 10a,b). Third, Shimizu (2024a) recently showed that the use of the vertical-mode amplitude of surface or isopycnal displacement as an objective function implicitly assumes omni-directional propagation of internal-wave signals in adjoint models. This implicit assumption might be relevant, because the PIL200 observations show that roughly one half of the VM1 internal-tide energy is associated with directional waves (but with large uncertainty; see Part I). Compared to omni-directional internal tides, internal tides propagating offshore would have higher sensitivity to remote sources in the straits between the Lesser Sunda Islands in Indonesia, although it would have lower sensitivity to remote sources on the Australian shelf. It would also be valuable to check the dependence of the results on mean background currents and realistic horizontal distribution of phase-speed variance and correlation length.

When comparing the results of this paper with other studies, it is important to remember that this study considered nonharmonic internal tides on a continental shelf, which is expected to have differences from those in deep ocean. The most important difference would be the roles played by higher modes. Table 2 shows that the highest three of the four lowest modes contribute roughly 1/4 of the total variance. It is likely that this relatively large contribution is caused by the fact that the PIL200 location is in the shelf/slope region, because the steep continental slope induces strong topographic interaction between VM1 and higher modes (e.g., see the excitation of VM2 in the immediate vicinity of the PIL200 location in Fig. 5b). For internal tides over an

abyssal plain, in contrast, VM1 and higher modes would propagate more independently, and a more relevant question would be whether the topographic conversion of higher modes to VM1 is substantial away from the observation location.

This study is the first study that took an "inverse" approach to the modelling of nonharmonic internal tides, and the results are promising. Since this is a feasibility study of the new modelling framework, there are many aspects of the model suite that can evolve in the future. For example, the adjoint frequency response analysis assumed linear dynamics, the standard ray theory was used despite potential inadequacies, only phase variability from travel-time variability along deterministic propagation paths was considered, and the stochastic model for the horizontal phase correlation was highly simplified. In principle, it would be possible to model relatively small variability of propagation paths and the along-path correlation of phase modulation based on the variance and correlation length of phase speed, which might make the empirical parameter for horizontal phase correlation α_r redundant (but the importance of the anisotropy of horizontal phase correlation would remain). Compared to the usual (forward) hydrodynamic modelling, the proposed model suite has complementary characteristics. The model suite focuses on a specific observation location and the statistics of nonharmonic internal tides. It does not yield information for the whole model domain or for a specific time; however, it yields information that is not straightforward to obtain from the usual hydrodynamic modelling, such as the contributions of different source regions (Fig. 9, Table 1), and the dependence on different processes and/or parameters (Fig. 10a,b), for nonharmonic internal tides from distributed sources. It is hoped that the proposed modelling framework provides a useful tool for studying nonharmonic internal tides in the future.

7 Conclusions

Together with Part I, this study developed a new framework and its implementation for process-based modelling of nonharmonic internal tides by combining adjoint, statistical, and stochastic approaches, and applied the resultant model suite to nonharmonic vertical-mode-one (VM1) semidiurnal internal tides at PIL200 location on the Australian North West Shelf. The proposed modelling framework provides a new tool for process-based studies of nonharmonic internal tides, when the superposition of many waves with different degrees of randomness makes process investigation difficult. Also, the combination of adjoint sensitivity modelling and the frequency response analysis from Fourier theory provides a new convenient way to calculate the deterministic sources of internal tides observed at a fixed location. The use of these methods led to the following new findings.

- The modelled nonharmonic internal-tide variance was not inconsistent with the observed variance for a realistic range of the model parameters, without considering the amplitude variability of the wave sources and the variability of wave propagation paths. This demonstrates the feasibility of the proposed modelling framework and model suite. This also means that, as a first approximation, nonharmonic internal tides are caused by phase-speed variability along the deterministic (or mean) propagation paths through travel time-induced phase modulation.

- Important parameters controlling nonharmonic internal-tide variance include the correlation length of phase speed and anisotropy of the horizontal correlation of phase modulation, in addition to phase-speed variance which has been identified in previous studies.

- The map of nonharmonic variance source function and its regional integrals provide a new convenient tool to identify important sources of nonharmonic internal tides. For the PIL200 location, important sources include the Australian North West Shelf away from the observation location, and the straits between the Lesser Sunda Islands in Indonesia, such as the Lombok Strait.

- Higher vertical modes can be important even when VM1 internal tide is analysed. In the example application, the highest three of the four lowest baroclinic modes contribute roughly 1/4 of the total variance.

- In addition to the above point, focusing only on VM1 and M_2 tidal constituent can lead to substantial underestimation of nonharmonic VM1 semidiurnal internal-tide variance, even when they are dominant. In the example application, VM1 and M_2 account for roughly a half of the total variance for the four lowest baroclinic modes and the four major semidiurnal constituents.

Data availability. Selected outputs of the model suite are available from Shimizu (2024b). (This data set can be accessed only by referees until the acceptance of this manuscript. Access instruction was provided to the editor.) The 2019 version of GEBCO bathymetry and the 2018 version of World Ocean Atlas are publicly available from https://www.gebco.net/data_and_products/gridded_bathymetry_data and https://www.ncei.noaa.gov/products/world-ocean-atlas, respectively. The version 5 of TPXO9-atlas was obtained from Dr. G. D. Egbert and Dr. S. Y. Erofeeva at Oregon State University, U.S.A.

Appendix A: Formulation of hydrodynamic model

The numerical hydrodynamic model used in this study is based on the vertical-mode decomposition of the governing equations over steep slopes, which was originally proposed by Griffiths and Grimshaw (2007) to my knowledge, and formulated in a more convenient form by Shimizu (2011, 2017, 2019). These studies used horizontally variable vertical modes, which are calculated using local water depth and background stratification. For example, using the generalized isopycnal coordinate s that depends only on density ρ and explicitly writing the horizontal vector components (unlike the main body of this paper, $\overrightarrow{x} = (x, y)$) for clarity, the isopycnal displacement η and the horizontal velocity (u, v) can be decomposed as (Shimizu, 2019)

$$\eta(x, y, s, t) = \sum_n \hat{\varphi}_n(x, y, s)\hat{\eta}_n(x, y, t), \tag{A1a}$$

$$u(x, y, s, t) = \sum_n \hat{\pi}_n(x, y, s)\hat{u}_n(x, y, t), \tag{A1b}$$

$$v(x, y, s, t) = \sum_n \hat{\pi}_n(x, y, s)\hat{v}_n(x, y, t), \tag{A1c}$$

where the sum is taken over all available vertical modes, $\hat{\eta}_n$, $\hat{u}_n$, and $\hat{v}_n$ are the nth vertical-mode amplitudes of the corresponding prognostic variable, and $\hat{\varphi}_n$ and $\hat{\pi}_n$ are the nth vertical modes for isopycnal displacement and horizontal velocity, respectively. Hereafter, the subscripts m and n denote vertical mode indices, which are 0 for the barotropic mode, 1 for the first baroclinic mode, etc. Each set of vertical modes $(\hat{\varphi}_n, \hat{\pi}_n)$ has the associated celerity c_n and normalization factor $\hat{h}_n$ with the unit of water depth. The normalization factor is defined as

$$\hat{\rho}\hat{h}_n = \int_{s^b}^{s^t} \hat{\pi}_n \rho \frac{dZ}{ds} \hat{\pi}_n ds, \tag{A2a}$$

where $\hat{\rho}$ is a reference density, and $Z(s)$ is the background height of isopycnal. Hereafter, the superscripts t and b denote the values at the surface and bottom, respectively. Since the choices of $\hat{\rho}$ and $\hat{h}_n$ are arbitrary, hat is used to denote variables whose magnitudes depend on these normalization factors.

For linear problems considered in this study, the multi-layer formulation in Shimizu (2011) and the continuous formulation in Shimizu (2019) become equivalent after vertical-mode decomposition. We assume linear and hydrostatic dynamics and $c_n \ll c_0$ for $n > 0$. Then, separating known barotropic (tidal) currents as external forcing, and neglecting other forcing and dissipation processes except linear bottom friction, the governing equations for $\hat{\eta}_n$, $\hat{u}_n$, and $\hat{v}_n$ for $n > 0$ are approximately given by

$$\frac{\partial \hat{\eta}_n}{\partial t} = -\frac{\partial}{\partial x}\left(\hat{h}_n \hat{u}_n\right) - \frac{\partial}{\partial y}\left(\hat{h}_n \hat{v}_n\right)$$
$$+ \sum_{m>0}\left(\hat{L}^x_{mn}\hat{h}_m\hat{u}_m + \hat{L}^y_{mn}\hat{h}_m\hat{v}_m\right) + \hat{f}^\eta_n, \tag{A3a}$$

$$\frac{\partial \hat{u}_n}{\partial t} = -\frac{\partial}{\partial x}\left(\frac{c_n^2}{\hat{h}_n}\hat{\eta}_n\right) - \sum_{m>0}\hat{L}^x_{nm}\frac{c_m^2}{\hat{h}_m}\hat{\eta}_m$$
$$+ f\hat{v}_n - \frac{1}{\hat{h}_n}\sum_{m>0}\hat{\Gamma}_{nm}\hat{u}_m, \tag{A3b}$$

$$\frac{\partial \hat{v}_n}{\partial t} = -\frac{\partial}{\partial y}\left(\frac{c_n^2}{\hat{h}_n}\hat{\eta}_n\right) - \sum_{m>0}\hat{L}^y_{nm}\frac{c_m^2}{\hat{h}_m}\hat{\eta}_m$$
$$- f\hat{u}_n - \frac{1}{\hat{h}_n}\sum_{m>0}\hat{\Gamma}_{nm}\hat{v}_m. \tag{A3c}$$

Here, $\hat{f}^\eta_n$ represents the forcing function from the barotropic to n^{th} baroclinic mode (shown in Fig. 2 for VM1 M$_2$ tide), $(\hat{L}^x_{nm}, \hat{L}^y_{nm})$ are topographic interaction coefficients, and $\hat{\Gamma}_{nm}$ are modal friction coefficients. These variables are defined as

$$\hat{f}^\eta_n = \hat{L}^x_{0n}\hat{h}_0\hat{u}_0 + \hat{L}^y_{0n}\hat{h}_0\hat{v}_0, \tag{A4a}$$

$$\hat{L}^x_{nm} = \frac{1}{\hat{\rho}\hat{h}_n}\int_{s^b}^{s^t} \hat{\pi}_n \rho \frac{dZ}{ds}\frac{\partial \hat{\pi}_m}{\partial x}ds, \tag{A4b}$$

$$\hat{\Gamma}_{nm} = \frac{\gamma}{\hat{\rho}}\hat{\pi}_n^b \rho^b \hat{\pi}_m^b, \tag{A4c}$$

where γ is the linear friction coefficient. The variable $\hat{L}_{nm}^y$ is defined similarly by replacing x by y in Eq. (A4b).

For numerical modelling, Eq. (A3) are discretized using the control volume (or finite volume) method on the staggered (or Arakawa-C) grid, assuming a sinusoidal motion with angular frequency ω. Then, the matrix operator is set-up for the model
925   state vector $[\hat{\eta}_1\ \hat{\eta}_2 \cdots \hat{u}_1\ \hat{u}_2 \cdots \hat{v}_1\ \hat{v}_2 \cdots]^T$, and the matrix operator is transposed to obtain the operator for the adjoint model, $\mathbf{L}^H$ in Eq. (21).

Author contributions. KS conceptualized this research, developed the methodology, conducted the formal analysis, investigation, and validation, visualized the results, and wrote and revised this paper.

Competing interests. The author has the following competing interests: Dr. Matt Rayson (editor) and other oceanographers at University of
930   Western Australia are involved in an on-going collaborative project with my company (involving myself) on the topic of this manuscript. Also, the author has a competitive relationship with them for industry-funded projects on topics related to this manuscript (in Australia).

Acknowledgements. This research was undertaken with the assistance of resources from the National Computational Infrastructure (NCI Australia), an NCRIS enabled capacity supported by the Australian Government. The original idea of the adjoint frequency response analysis was developed while KS was at Max Planck Institute for Meteorology under the financial support by the Max Planck Society for the
935   Advancement of Science through the Klaus Hasselmann Postdoctoral Fellowship. KS thanks Jochem Marotzke for introduction to adjoint modelling. KS also thanks Steve Buchan for proof reading.

References

Alford, M. H., Simmons, H. L., Marques, O. B., and Girton, J. B.: Internal tide attenuation in the North Pacific, Geophys. Res. Lett., 46, 8205–8213, https://doi.org/10.1029/2019GL082648, 2019.

940 Bennett, A. F.: Inverse Modeling of the Ocean and Atmosphere, Cambridge University Press, 2002.

Blayo, E. and Debreu, L.: Revisiting open boundary conditions from the point of view of characteristic variables, Ocean Model., 9, 231–252, https://doi.org/10.1016/j.ocemod.2004.07.001, 2005.

Buijsman, M. C., Arbic, B. K., Richman, J. G., Shriver, J. F., Wallcraft, A. J., and Zamudio, L.: Semidiurnal internal tide incoherence in the equatorial Pacific, J. Geophys. Res.: Oceans, 122, 5286–5305, https://doi.org/10.1002/2016JC012590, 2017.

945 Colosi, J. A.: Sound Propagation through the Stochastic Ocean, Cambridge University Press, 2016.

Colosi, J. A. and Munk, W.: Tales of the venerable Honolulu tide gauge, J. Phys. Oceanogr., 36, 967–996, https://doi.org/10.1175/JPO2876.1, 2006.

Egbert, G. D. and Erofeeva, S. Y.: Efficient inverse modeling of barotropic ocean tides, J. Atmos. Oceanic Tech., 19, 183–204, https://doi.org/10.1175/1520-0426(2002)019<0183:EIMOBO>2.0.CO;2, 2002.

950 Flather, R. A.: A tidal model of the northwest European continental shelf, Mem. Soc. Roy. Sci. Liege, 10, 141–164, 1976.

GEBCO Compilation Group: GEBCO 2019 Grid, https://doi.org/10.5285/836f016a-33be-6ddc-e053-6c86abc0788e, 2019.

Geoffroy, G. and Nycander, J.: Global mapping of the nonstationary semidiurnal internal tide using Argo data, J. Geophys. Res.: Oceans, 127, e2021JC018 283, https://doi.org/10.1029/2021JC018283, 2022.

Griffiths, S. D. and Grimshaw, R. H. J.: Internal tide generation at the continental shelf modeled using a modal decomposition: Two-

955 dimensional results, J. Phys. Oceanogr., 37, 428–451, https://doi.org/10.1175/JPO3068.1, 2007.

Kerry, C. G., Powell, B. S., and Carter, G. S.: Quantifying the incoherent M_2 internal tide in the Philippine Sea, J. Phys. Oceanogr., 46, 2483–2491, https://doi.org/10.1175/JPO-D-16-0023.1, 2016.

Klocker, A. and Abernathey, R.: Global patterns of mesoscale eddy properties and diffusivities, J. Phys. Oceanogr., 44, 1030–1046, https://doi.org/10.1175/JPO-D-13-0159.1, 2014.

960 Lighthill, J.: Waves in Fluids, Cambridge University Press, 1978.

Locarnini, R. A., Mishonov, A. V., Baranova, O. K., Boyer, T. P., Zweng, M. M., Garcia, H. E., Reagan, J. R., Seidov, D., Weathers, K., Paver, C. R., and Smolyar, I.: World Ocean Atlas 2018, Volume 1: Temperature, in: NOAA Atlas NESDIS, edited by Mishonov, A., vol. 81, p. 52, 2018.

Marotzke, J., Giering, R., Zhang, K. Q., Stammer, D., Hil, C., and Lee, T.: Construction of the adjoint MIT ocean gen-

965 eral circulation model and application to Atlantic heat transport sensitivity, J. Geophys. Res.: Oceans, 104, 29 529–29 547, https://doi.org/10.1029/1999JC900236, 1999.

McDougall, T. J. and Barker, P. M.: Getting started with TEOS-10 and Gibbs Sea Water (GSW) oceanographic toolbox, p. 28, SCOR/IAPSO WG127, 2011.

Park, J.-H. and Watts, D. R.: Internal tides in the southwestern Japan/East Sea, J. Phys. Oceanogr., 36, 22–34,

970 https://doi.org/10.1175/JPO2846.1, 2006.

Rainville, L. and Pinkel, R.: Propagation of low-mode internal waves through the ocean, J. Phys. Oceanogr., 36, 1220–1236, https://doi.org/10.1175/JPO2889.1, 2006.

Särkkä, S. and Solin, A.: Applied Stochastic Differential Equations, Cambridge University Press, 2019.

Shimizu, K.: A theory of vertical modes in multilayer stratified fluids, J. Phys. Oceanogr., 41, 1694–1707, https://doi.org/10.1175/2011JPO4546.1, 2011.

Shimizu, K.: Physical uniqueness of higher-order Korteweg-de Vries theory for continuously stratified fluids without background shear, Phys. Fluids, 29, 106 604, https://doi.org/10.1063/1.5008767, 2017.

Shimizu, K.: Fully nonlinear simple internal waves over subcritical slopes in continuously stratified fluids: Theoretical development, Phys. Fluids, 31, 016 601, https://doi.org/10.1063/1.5074095, 2019.

Shimizu, K.: Fundamental properties of adjoint model and adjoint sensitivity under fully nonlinear hydrostatic internal gravity waves, J. Geophys. Res.: Oceans, 129, e2023JC020 577, https://doi.org/10.1029/2023JC020577, 2024a.

Shimizu, K.: Data from: Process-based modelling of nonharmonic internal tides using adjoint, statistical, and stochastic approaches. Part II: adjoint frequency response analysis, stochastic models, and synthesis, Zenodo, https://doi.org/10.5281/zenodo.13999971, (This data set can be accessed only by referees until the acceptance of this manuscript. Access instruction was provided to the editor.), 2024b.

Shimizu, K.: Process-based modelling of nonharmonic internal tides using adjoint, statistical, and stochastic approaches. Part I: statistical model and analysis of observational data, Ocean Sci., Companion Paper.

Weaver, A. and Courtier, P.: Correlation modelling on the sphere using a generalized diffusion equation, Q. J. R. Meteorol. Soc., 127, 1815–1846, https://doi.org/10.1002/qj.49712757518, 2001.

Wunsch, C.: The vertical partition of oceanic horizontal kinetic energy, J. Phys. Oceanogr., 27, 1770–1794, https://doi.org/10.1175/1520-0485(1997)027<1770:TVPOOH>2.0.CO;2, 1997.

Wunsch, C.: Discrete Inverse and State Estimation Problems, Cambridge University Press, 2006.

Zaron, E. D. and Egbert, G. D.: Time-variable refraction of the internal tide at the Hawaiian Ridge, J. Phys. Oceanogr., 44, 538–557, https://doi.org/10.1175/JPO-D-12-0238.1, 2014.

Zweng, M. M., Reagan, J. R., Seidov, D., Boyer, T. P., Locarnini, R. A., Garcia, H. E., Mishonov, A. V., Baranova, O. K., Weathers, K., Paver, C. R., and Smolyar, I.: World Ocean Atlas 2018, Volume 2: Salinity, in: NOAA Atlas NESDIS, edited by Mishonov, A., vol. 82, p. 50, 2018.